Available online at www.sciencedirect.com
ScienceDirect
Comput. Methods Appl. Mech. Engrg. 416 (2023) 116325
Computer methods in applied mechanics and engineering
www.elsevier.com/locate/cma

A mixed integration point (MIP) formulation for hyperelastic Kirchhoff–Love shells for nonlinear static and dynamic analysis

Leonardo Leonetti[a,b,*], Josef Kiendl[c]

[a] Dipartimento di Ingegneria Informatica, Modellistica, Elettronica e Sistemistica, Università della Calabria, Italy
[b] CIRTech Institute, Ho Chi Minh City University of Technology (HUTECH), Ho Chi Minh City, Viet Nam
[c] Institute of Engineering Mechanics and Structural Analysis, Universität der Bundeswehr München, Munich, Germany

Received 25 May 2023; received in revised form 24 July 2023; accepted 26 July 2023
Available online xxxx

Abstract

We present a mixed integration point (MIP) formulation for hyperelastic isogeometric Kirchhoff–Love shells. While previous works have proposed mixed integration point schemes for different structural formulations in the context of geometric nonlinearity, we extend this concept to the large strain regime in this paper. The non-trivial extension to the nonlinear dynamic analysis for these materials based on the one-step energy-conserving method is also proposed. We present a general, consistent derivation of the formulation, which is not restricted to Kirchhoff–Love shells, hyperelastic materials, or isogeometric analysis, but can be applied to any structural problem involving geometric and material nonlinearities. Several numerical benchmark examples demonstrate the applicability and efficiency of the method.

Keywords: Mixed integration point; Material nonlinearity; Hyperelasticity; Isogeometric analysis; Kirchhoff–love shells

1. Introduction

It is well known that in path-following methods [1] for geometrically nonlinear analyses mixed formulations [2], which consider both displacements and stresses as primary variables, perform better than displacement-based formulations in terms of robustness and efficiency regarding the necessary number of load steps [3–5].

On the other hand, mixed formulations are typically more complex than displacement-based ones, require a careful choice of the discretization spaces for the different fields, and can be numerically expensive due to he additional fields to be discretized and solved for. The latter aspect is true especially for higher-order methods like isogeometric analysis (IGA) [6]. In low-order finite element mixed methods, the stress fields may be discretized by discontinuous functions which allows a static condensation of the additional unknowns at the element level. For higher-order finite element and isogeometric mixed formulations, this is in general not possible, leading to a highly increased computational effort [7,8]. For these reasons, the so-called Mixed Integration Point (MIP) strategy has been recently proposed in [9] as an effort to obtain the improved behavior of mixed methods as described above within the framework of displacement-based formulations. The main idea is to introduce additional stress

* Corresponding author at: Dipartimento di Ingegneria Informatica, Modellistica, Elettronica e Sistemistica, Università della Calabria, Italy.
E-mail addresses: leonardo.leonetti@unical.it (L. Leonetti), josef.kiendl@unibw.de (J. Kiendl).

https://doi.org/10.1016/j.cma.2023.116325

variables locally at each integration point, which can then be eliminated by static condensation from the global equation system, such that the variables to be discretized and solved for are the same as in a displacement-based formulation. This represents a relaxation of the constitutive equations at each integration point during the Newton iterative process.

The MIP concept was firstly proposed in the context of IGA in [10] for solid-shells, then in [11–13] for shells, and in [14–17] for spatial beams. Furthermore, it was successfully applied to Koiter post-buckling analysis [18], thermoelastic analysis of shells [19], small strain plasticity in beams and shells [20], and in the context of reduced order models for the optimal design of shells undergoing buckling with imperfection sensitivity [21–24].

With this paper, we extend the application of the MIP concept from geometrically nonlinear problems to fully nonlinear problems including large strains, considering a hyperelastic Kirchhoff–Love shell formulation [25].

The formulation is derived consistently for a general nonlinear structural problem, and could, therefore, easily be adapted to other formulations, for example solid-shell models [26–29]. In this context, we also investigate the applicability of the simplified Kirchhoff–Love shell formulation proposed in [30] to the large strain regime. Furthermore, we extend the concept to dynamic problems by combining the MIP formulation with a one-step energy-conserving time integration method originally proposed in [31], based on the concepts for energy conservation [32–36].

The paper is structured as follows. In Section 2, we review the isogeometric hyperelastic Kirchhoff–Love shell model [25], modified for the simplified bending strain measure [30]. We rewrite the formulation from [25] in a different form, which provides the basis for the MIP formulation presented in Section 3. Section 4 shows the combination of the formulation with the time integration scheme from [31], and Section 5 tests the presented formulations on different static and dynamic benchmark problems. Finally, we draw conclusions in Section 6.

2. Hyperelastic Kirchhoff–Love shell formulation with simplified bending strain

In this section, we summarize the governing equations of a hyperelastic Kirchhoff–Love shell model as proposed in [25], modified for the simplified bending strain measure initially proposed in [30]. This model is the basis for the newly proposed MIP formulation presented in the next section.

2.1. Governing equations

For presenting the governing equations, we employ index notation with Latin indices taking on values $\{1, 2, 3\}$, while Greek indices take on values $\{1, 2\}$, and summation convention of repeated indices is used. A shell's convective curvilinear coordinates are denoted by θ^i, where θ^α are the surface coordinates and θ^3 is the thickness coordinate. Partial derivatives with respect to θ^i are indicated as $(\cdot)_{,i} = \partial(\cdot)/\partial\theta^i$. Deformation is generally described through geometric quantities in deformed and undeformed configurations, where variables of the undeformed configuration are indicated by $\mathring{(\cdot)}$.

Given a point $\mathring{\mathbf{r}}$ on the midsurface of the reference configuration, the tangent base vectors $\mathring{\mathbf{a}}_\alpha$ and the unit normal vector $\mathring{\mathbf{a}}_3$ of the midsurface are obtained as

$$\mathring{\mathbf{a}}_\alpha = \mathring{\mathbf{r}}_{,\alpha} \ , \tag{1}$$

$$\mathring{\mathbf{a}}_3 = \frac{\mathring{\mathbf{a}}_1 \times \mathring{\mathbf{a}}_2}{\left|\mathring{\mathbf{a}}_1 \times \mathring{\mathbf{a}}_2\right|} \ . \tag{2}$$

A point in the shell body off the midsurface is denoted by $\mathring{\mathbf{x}}$ and is related to the corresponding point on the midsurface $\mathring{\mathbf{r}}$ via the normal vector as

$$\mathring{\mathbf{x}} = \mathring{\mathbf{r}} + \theta^3 \, \mathring{\mathbf{a}}_3 \ , \tag{3}$$

with $-h/2 \leq \theta^3 \leq h/2$, h being the shell thickness. The base vectors at a point in the shell body are denoted by $\mathring{\mathbf{g}}_i = \mathring{\mathbf{x}}_{,i}$ and can be expressed by those of the midsurface $\mathring{\mathbf{a}}_i$ as follows

$$\mathring{\mathbf{g}}_\alpha = \mathring{\mathbf{a}}_\alpha + \theta^3 \, \mathring{\mathbf{a}}_{3,\alpha} \ , \tag{4}$$

$$\mathring{\mathbf{g}}_3 = \mathbf{a}_3 \ . \tag{5}$$

The first and second fundamental forms of the midsurface yield the metric and curvature coefficients

$$\mathring{a}_{\alpha\beta} = \mathring{\mathbf{a}}_\alpha \cdot \mathring{\mathbf{a}}_\beta \ , \tag{6}$$

$$\mathring{b}_{\alpha\beta} = \mathring{\mathbf{a}}_{\alpha,\beta} \cdot \mathring{\mathbf{a}}_3 \ . \tag{7}$$

The metric coefficients at a point in the shell continuum are then obtained as

$$\mathring{g}_{\alpha\beta} = \mathring{a}_{\alpha\beta} - 2\theta^3 b_{\alpha\beta} + \left(\theta^3\right)^2 \mathring{\mathbf{a}}_{3,\alpha} \cdot \mathring{\mathbf{a}}_{3,\beta} \ , \tag{8}$$

$$\mathring{g}_{\alpha 3} = \mathring{g}_{3\alpha} = \mathring{\mathbf{a}}_\alpha \cdot \mathring{\mathbf{a}}_3 + \theta^3 \mathring{\mathbf{a}}_{3,\alpha} \cdot \mathring{\mathbf{a}}_3 = 0 \ , \tag{9}$$

$$\mathring{g}_{33} = \mathring{a}_{33} = 1 \ . \tag{10}$$

Corresponding to the classical assumption of a linear strain distribution through the thickness, the quadratic term in Eq. (8) is neglected

$$\mathring{g}_{\alpha\beta} = \mathring{a}_{\alpha\beta} - 2\theta^3 \mathring{b}_{\alpha\beta} \ . \tag{11}$$

The displacement vector $\mathbf{u}$ describes the deformation of a point on the midsurface from the undeformed to the deformed configuration $\mathbf{r} = \mathring{\mathbf{r}} + \mathbf{u}$, and Eqs. (1)–(11) can be applied identically to the actual configurations. However, in this work, we adopt the approximation of the unit normal vector in the deformed configuration as proposed in [30]

$$\mathbf{a}_3 = \frac{\mathbf{a}_1 \times \mathbf{a}_2}{\left|\mathring{\mathbf{a}}_1 \times \mathring{\mathbf{a}}_2\right|} \ , \tag{12}$$

which is then used for computing the curvature coefficients of the midsurface in the deformed configuration. This approximation reduces the nonlinearity of the strain measure and simplifies its linearization, as has been shown in [30], where it was tested successfully for geometrically nonlinear problems. In the numerical examples of the present paper, we investigate the accuracy of this simplified strain measure in the context of hyperelastic large-strain problems.

The metric coefficients (11) in the current configuration represent also the in-plane components of the right Cauchy–Green deformation tensor $C_{\alpha\beta} = g_{\alpha\beta}$, while $C_{\alpha 3} = g_{\alpha 3} = 0$. The thickness deformation $C_{33} \neq g_{33}$ cannot be obtained directly from the shell kinematics but needs to be recovered through the constitutive equations by enforcing the plane stress condition, as briefly summarized in the following. Assuming an arbitrary hyperelastic material, described by a strain energy function ψ, the second Piola–Kirchhoff stress tensor S^{ij} and the tangent material tensor $\mathbb{C}^{ijkl}$ are defined as

$$S^{ij} = 2\frac{\partial \psi}{\partial C_{ij}} \ , \tag{13}$$

$$\mathbb{C}^{ijkl} = 4\frac{\partial^2 \psi}{\partial C_{ij} \partial C_{kl}} \ . \tag{14}$$

An incorrect assumption of C_{33} would lead to a violation of the plane stress assumption $S^{33} = 0$. In turn, the plane stress condition can be used to determine the thickness deformation by an iterative correction as follows [25]

$$\Delta C_{33}^{(I)} = -2\frac{S_{(I)}^{33}}{\mathbb{C}_{(I)}^{3333}} \ , \tag{15}$$

$$C_{33}^{(I+1)} = C_{33}^{(I)} + \Delta C_{33}^{(I)} \ , \tag{16}$$

where I indicates the iteration step. With the updated C_{33}, the updates of S^{ij} and $\mathbb{C}^{ijkl}$ are computed until the plane stress condition is satisfied up to a specified tolerance. In the case of incompressible materials, the correction of C_{33} can also be done analytically, leading to the following expressions for the stress and material tensors

$$S^{ij} = 2\frac{\partial \psi_{el}}{\partial C_{ij}} - 2\frac{\partial \psi_{el}}{\partial C_{33}} C_{33} \bar{C}^{ij} \ , \tag{17}$$

$$\begin{aligned} \mathbb{C}^{ijkl} = {} & 4\frac{\partial^2 \psi_{el}}{\partial C_{ij} \partial C_{kl}} - 2\frac{\partial \psi_{el}}{\partial C_{33}} C_{33} (\bar{C}^{ij} \bar{C}^{kl} - \bar{C}^{ik} \bar{C}^{jl} - \bar{C}^{il} \bar{C}^{jk}) \\ & - 4\left(\frac{\partial^2 \psi_{el}}{\partial C_{33} \partial C_{ij}} C_{33} + \frac{\partial \psi_{el}}{\partial C_{33}} \delta^{i3} \delta^{j3} \right) \bar{C}^{kl} - 4\bar{C}^{ij} \left(\frac{\partial^2 \psi_{el}}{\partial C_{33} \partial C_{kl}} C_{33} + \frac{\partial \psi_{el}}{\partial C_{33}} \delta^{k3} \delta^{l3} \right) \ , \end{aligned} \tag{18}$$

where ψ_{el} is the elastic part of the strain energy function without the incompressibility constraint, $\bar{C}^{ij}$ are the components of the inverse of the deformation tensor, δ^{i3} is the Kronecker Delta, and J_o is the in-plane Jacobian determinant defined by

$$J_o = \sqrt{\frac{|g_{\alpha\beta}|}{|\mathring{g}_{\alpha\beta}|}} \ . \tag{19}$$

In the expressions Eqs. (17)–(18), both the incompressibility constraint and plane stress constraint are already satisfied, for more details, reference is made to [25]. With the plane stress condition ensured, the statically condensed material tensor $\hat{\mathbb{C}}^{\alpha\beta\gamma\delta}$ can be obtained as

$$\hat{\mathbb{C}}^{\alpha\beta\gamma\delta} = \mathbb{C}^{\alpha\beta\gamma\delta} - \frac{\mathbb{C}^{\alpha\beta 33}\mathbb{C}^{33\gamma\delta}}{\mathbb{C}^{3333}} \ , \tag{20}$$

and only in-plane stress and strain components need to be considered. As strain measure, we use the Green–Lagrange strain obtained as

$$E_{\alpha\beta} = \frac{1}{2}(g_{\alpha\beta} - \mathring{g}_{\alpha\beta}) \tag{21}$$

$$= \frac{1}{2}\left((a_{\alpha\beta} - \mathring{a}_{\alpha\beta}) - 2\theta^3(b_{\alpha\beta} - \mathring{b}_{\alpha\beta})\right) \tag{22}$$

$$= \varepsilon_{\alpha\beta} + \theta^3\kappa_{\alpha\beta} \ . \tag{23}$$

Stresses are integrated over the thickness, yielding the stress resultants

$$n^{\alpha\beta} = \int_{-h/2}^{h/2} S^{\alpha\beta}\mathrm{d}\theta^3 \ , \tag{24}$$

$$m^{\alpha\beta} = \int_{-h/2}^{h/2} S^{\alpha\beta}\theta^3\mathrm{d}\theta^3 \ , \tag{25}$$

representing membrane forces and moments, respectively. For their total differentials, we obtain

$$\mathrm{d}n^{\alpha\beta} = \left(\int_{-h/2}^{h/2} \hat{\mathbb{C}}^{\alpha\beta\gamma\delta}\mathrm{d}\theta^3\right)\mathrm{d}\varepsilon_{\gamma\delta} + \left(\int_{-h/2}^{h/2} \hat{\mathbb{C}}^{\alpha\beta\gamma\delta}\,\theta^3\mathrm{d}\theta^3\right)\mathrm{d}\kappa_{\gamma\delta} \ , \tag{26}$$

$$\mathrm{d}m^{\alpha\beta} = \left(\int_{-h/2}^{h/2} \hat{\mathbb{C}}^{\alpha\beta\gamma\delta}\theta^3\mathrm{d}\theta^3\right)\mathrm{d}\varepsilon_{\gamma\delta} + \left(\int_{-h/2}^{h/2} \hat{\mathbb{C}}^{\alpha\beta\gamma\delta}(\theta^3)^2\,\mathrm{d}\theta^3\right)\mathrm{d}\kappa_{\gamma\delta} \ . \tag{27}$$

It should be noted that in Eqs. (26)–(27) only $\hat{\mathbb{C}}^{\alpha\beta\gamma\delta}$ need to be integrated through the thickness, while strain variables are expressed by the midsurface variables $\mathrm{d}\varepsilon_{\gamma\delta}$ and $\mathrm{d}\kappa_{\gamma\delta}$.

The variational formulation of the problem is obtained from the equilibrium of internal and external virtual work, $\delta W^{int} = \delta W^{ext}$, with internal and external virtual work defined as

$$\delta W^{int} = \int_A (\mathbf{n} : \delta\boldsymbol{\varepsilon} + \mathbf{m} : \delta\boldsymbol{\kappa})\ \mathrm{d}A \ , \tag{28}$$

$$\delta W^{ext} = \int_A \mathbf{f}\cdot\delta\mathbf{u}\,\mathrm{d}A \ , \tag{29}$$

where $\delta\mathbf{u}$ is a virtual displacement, $\delta\boldsymbol{\varepsilon}$ and $\delta\boldsymbol{\kappa}$ are the corresponding virtual membrane strain and change in curvature, respectively, while $\mathbf{f}$ denotes the external load. A denotes the midsurface and $\mathrm{d}A = \sqrt{|\mathring{a}_{\alpha\beta}|}\mathrm{d}\theta^1\mathrm{d}\theta^2$ the differential area, both in the reference configuration.

2.2. Discretization and linearization

The displacement vector is discretized as

$$\mathbf{u} = \sum_a^{n_{sh}} N^a\mathbf{u}^a \ , \tag{30}$$

where N^a are the shape functions, with n_{sh} as the total number of shape functions, and $\mathbf{u}^a$ are the nodal displacement vectors with the components u_i^a $(i = 1, 2, 3)$ referring to the global $x-$, $y-$, $z-$components. The global degree of freedom number r of a nodal displacement is defined by $r = 3(a-1)+i$, such that $u_r = u_i^a$. The variation with respect to u_r is obtained by the partial derivative $\partial/\partial u_r$

$$\frac{\partial \mathbf{u}}{\partial u_r} = N^a \mathbf{e}_i \ . \tag{31}$$

Similar to Eq. (31), the variations of derived variables, such as strains, with respect to u_r can be obtained, which is shown in detail in [25]. The variations of δW^{int} and δW^{ext} with respect to u_r yield the vectors of internal and external nodal forces, with F_r^{int} and F_r^{ext} representing their rth component

$$F_r^{int} = \int_A \left(\mathbf{n} : \frac{\partial \boldsymbol{\varepsilon}}{\partial u_r} + \mathbf{m} : \frac{\partial \boldsymbol{\kappa}}{\partial u_r} \right) \mathrm{d}A \ , \tag{32}$$

$$F_r^{ext} = \int_A \mathbf{f} \cdot \frac{\partial \mathbf{u}}{\partial u_r} \mathrm{d}A \ . \tag{33}$$

Linearizing Eq. (32), we obtain the components of the tangential stiffness matrix

$$K_{rs} = \int_A \left(\frac{\partial \mathbf{n}}{\partial u_s} : \frac{\partial \boldsymbol{\varepsilon}}{\partial u_r} + \frac{\partial \mathbf{m}}{\partial u_s} : \frac{\partial \boldsymbol{\kappa}}{\partial u_r} + \mathbf{n} : \frac{\partial^2 \boldsymbol{\varepsilon}}{\partial u_r \partial u_s} + \mathbf{m} : \frac{\partial^2 \boldsymbol{\kappa}}{\partial u_r \partial u_s} \right) \mathrm{d}A \ . \tag{34}$$

Finally, we write the linearized equation system which is solved for the incremental displacement vector $\dot{\mathbf{u}}$

$$\mathbf{K}\,\dot{\mathbf{u}} = -\mathbf{R} \ , \tag{35}$$

with $\mathbf{R} = \mathbf{F}^{int} - \mathbf{F}^{ext}$ being the residual vector.

As the curvature-related terms in the internal force vector and stiffness matrix involve second derivatives of the displacement, a C^1-continuous discretization is necessary. In this paper, we use NURBS-based isogeometric analysis [6]. The details of the linearization of $\boldsymbol{\varepsilon}$ and $\boldsymbol{\kappa}$ with respect to u_r, u_s are presented in [25].

For implementation, we rewrite the relevant tensors in Voigt notation as follows

$$\overline{\mathbf{n}} = \begin{pmatrix} n^{11} \\ n^{22} \\ n^{12} \end{pmatrix} \ , \qquad \overline{\mathbf{m}} = \begin{pmatrix} m^{11} \\ m^{22} \\ m^{12} \end{pmatrix} \ , \qquad \overline{\boldsymbol{\varepsilon}} = \begin{pmatrix} \varepsilon_{11} \\ \varepsilon_{22} \\ 2\,\varepsilon_{12} \end{pmatrix} \ , \qquad \overline{\boldsymbol{\kappa}} = \begin{pmatrix} \kappa_{11} \\ \kappa_{22} \\ 2\,\kappa_{12} \end{pmatrix} \ , \tag{36}$$

and the material tensor represented as a 3×3 material matrix:

$$\overline{\mathbf{D}} = \begin{pmatrix} \hat{\mathbb{C}}^{1111} & \hat{\mathbb{C}}^{1122} & \hat{\mathbb{C}}^{1112} \\ & \hat{\mathbb{C}}^{2222} & \hat{\mathbb{C}}^{2212} \\ symm. & & \hat{\mathbb{C}}^{1212} \end{pmatrix} \ . \tag{37}$$

Furthermore, we introduce the following thickness-integrated material matrices:

$$\overline{\mathbf{D}}^0 = \int_{-h/2}^{h/2} \overline{\mathbf{D}} \, \mathrm{d}\theta^3 \ , \qquad \overline{\mathbf{D}}^1 = \int_{-h/2}^{h/2} \theta^3 \overline{\mathbf{D}} \, \mathrm{d}\theta^3 \ , \qquad \overline{\mathbf{D}}^2 = \int_{-h/2}^{h/2} \left(\theta^3\right)^2 \overline{\mathbf{D}} \, \mathrm{d}\theta^3 \ , \tag{38}$$

such that Eqs. (26)–(27) can be rewritten as:

$$\mathrm{d}\overline{\mathbf{n}} = \overline{\mathbf{D}}^0 \, \mathrm{d}\overline{\boldsymbol{\varepsilon}} + \overline{\mathbf{D}}^1 \, \mathrm{d}\overline{\boldsymbol{\kappa}} \ , \tag{39}$$

$$\mathrm{d}\overline{\mathbf{m}} = \overline{\mathbf{D}}^1 \, \mathrm{d}\overline{\boldsymbol{\varepsilon}} + \overline{\mathbf{D}}^2 \, \mathrm{d}\overline{\boldsymbol{\kappa}} \ . \tag{40}$$

Finally, we can write the internal forces (32) and stiffness matrix (34) components as:

$$F_r^{int} = \int_A \left(\overline{\mathbf{n}}^T \frac{\partial \overline{\boldsymbol{\varepsilon}}}{\partial u_r} + \overline{\mathbf{m}}^T \frac{\partial \overline{\boldsymbol{\kappa}}}{\partial u_r} \right) \mathrm{d}A \ , \tag{41}$$

$$K_{rs} = \int_A \left(\left(\overline{\mathbf{D}}^0 \frac{\partial \overline{\boldsymbol{\varepsilon}}}{\partial u_s} + \overline{\mathbf{D}}^1 \frac{\partial \overline{\boldsymbol{\kappa}}}{\partial u_s} \right)^T \frac{\partial \overline{\boldsymbol{\varepsilon}}}{\partial u_r} + \overline{\mathbf{n}}^T \frac{\partial^2 \overline{\boldsymbol{\varepsilon}}}{\partial u_r \partial u_s} + \left(\overline{\mathbf{D}}^1 \frac{\partial \overline{\boldsymbol{\varepsilon}}}{\partial u_s} + \overline{\mathbf{D}}^2 \frac{\partial \overline{\boldsymbol{\kappa}}}{\partial u_s} \right)^T \frac{\partial \overline{\boldsymbol{\kappa}}}{\partial u_r} + \overline{\mathbf{m}}^T \frac{\partial^2 \overline{\boldsymbol{\kappa}}}{\partial u_r \partial u_s} \right) \mathrm{d}A \ . \tag{42}$$

The stiffness matrix formulation (42) can be split into two parts, which are typically denoted as the material and geometric stiffness matrices, $\mathbf{K}^{mat}$ and $\mathbf{K}^{geo}$, respectively, as follows

$$K_{rs}^{mat} = \int_A \left(\left(\overline{\mathbf{D}}^0 \frac{\partial \overline{\boldsymbol{\varepsilon}}}{\partial u_s} + \overline{\mathbf{D}}^1 \frac{\partial \overline{\boldsymbol{\kappa}}}{\partial u_s} \right)^T \frac{\partial \overline{\boldsymbol{\varepsilon}}}{\partial u_r} + \left(\overline{\mathbf{D}}^1 \frac{\partial \overline{\boldsymbol{\varepsilon}}}{\partial u_s} + \overline{\mathbf{D}}^2 \frac{\partial \overline{\boldsymbol{\kappa}}}{\partial u_s} \right)^T \frac{\partial \overline{\boldsymbol{\kappa}}}{\partial u_r} \right) \mathrm{d}A \ , \tag{43}$$

$$K_{rs}^{geo} = \int_A \left(\overline{\mathbf{n}}^T \frac{\partial^2 \overline{\boldsymbol{\varepsilon}}}{\partial u_r \partial u_s} + \overline{\mathbf{m}}^T \frac{\partial^2 \overline{\boldsymbol{\kappa}}}{\partial u_r \partial u_s} \right) \mathrm{d}A \ , \tag{44}$$

with $\mathbf{K} = \mathbf{K}^{mat} + \mathbf{K}^{geo}$.

For a more compact notation of (41)–(44), we introduce the following generalized vectors for the stress resultants and the strain variables

$$\mathbf{t} = \begin{pmatrix} \overline{\mathbf{n}} \\ \overline{\mathbf{m}} \end{pmatrix} \ , \qquad \boldsymbol{\rho} = \begin{pmatrix} \overline{\boldsymbol{\varepsilon}} \\ \overline{\boldsymbol{\kappa}} \end{pmatrix} \ , \tag{45}$$

and the variations of the latter with respect to u_r, u_s

$$\boldsymbol{\rho}_{,r} = \begin{pmatrix} \frac{\partial \overline{\boldsymbol{\varepsilon}}}{\partial u_r} \\ \frac{\partial \overline{\boldsymbol{\kappa}}}{\partial u_r} \end{pmatrix} \ , \qquad \boldsymbol{\rho}_{,rs} = \begin{pmatrix} \frac{\partial^2 \overline{\boldsymbol{\varepsilon}}}{\partial u_r \partial u_s} \\ \frac{\partial^2 \overline{\boldsymbol{\kappa}}}{\partial u_r \partial u_s} \end{pmatrix} \ . \tag{46}$$

Furthermore, we gather the first variations of the strain variables in a strain–displacement matrix $\mathbf{B}$

$$\mathbf{B} = \begin{pmatrix} \boldsymbol{\rho}_{,1} & \boldsymbol{\rho}_{,2} & \dots & \boldsymbol{\rho}_{,ndof} \end{pmatrix} \ , \tag{47}$$

noting that $\mathbf{B}$ is still a function of the displacements $\mathbf{u}$, and we define the 6×6 material matrix $\mathbf{D}$

$$\mathbf{D} = \begin{pmatrix} \overline{\mathbf{D}}^0 & \overline{\mathbf{D}}^1 \\ \overline{\mathbf{D}}^1 & \overline{\mathbf{D}}^2 \end{pmatrix} \ , \tag{48}$$

where $\overline{\mathbf{D}}^0, \overline{\mathbf{D}}^1, \overline{\mathbf{D}}^2$ are the thickness-integrated material matrices defined in (38).

With (45)–(48), Eqs. (39)–(44) can be rewritten in a more compact and general form, which can easily be applied to other structural formulations. Eqs. (39)–(40) turn into a single equation

$$\mathbf{D}\mathrm{d}\boldsymbol{\rho} = \mathrm{d}\mathbf{t} \ , \tag{49}$$

and the expressions for internal forces (41) and stiffness matrices (43)–(44) can be written in a as follows

$$\mathbf{F}^{int} = \int_A \mathbf{B}^T \mathbf{t} \, \mathrm{d}A \ , \tag{50}$$

$$\mathbf{K}^{mat} = \int_A \mathbf{B}^T \mathbf{D} \mathbf{B} \, \mathrm{d}A \ , \tag{51}$$

$$\mathbf{K}^{geo} = \int_A \mathbf{k}^{geo} \, \mathrm{d}A \ , \tag{52}$$

$$k_{rs}^{geo} = \mathbf{t}^T \boldsymbol{\rho}_{,rs} \ . \tag{53}$$

The integrals in (50)–(52) are evaluated by numerical quadrature

$$\mathbf{F}^{int} = \sum_{i=1}^{N_s} \mathbf{B}_i^T \mathbf{t}_i \, w_i \tag{54}$$

$$\mathbf{K}^{mat} = \sum_{i=1}^{N_s} \mathbf{B}_i^T \mathbf{D}_i \mathbf{B}_i \, w_i \ , \tag{55}$$

$$\mathbf{K}^{geo} = \sum_{i=1}^{N_s} \mathbf{k}_i^{geo} \, w_i \ , \tag{56}$$

with the subscript i indicating quantities evaluated at an integration point, N_s as the number of integration points, and w_i as the corresponding integration weights. Eqs. (54)–(56) provide the basis for the derivation of the MIP formulation in the next section.

3. The iterative scheme with mixed integration points (MIP)

The motivation of the MIP approach is the fact that standard displacement formulations may exhibit poor robustness in the iterative solution scheme obtained via a standard Newton linearization in certain problem classes, like, e.g., thin shells, limiting the allowable load (or arc-length) step size and, by this, increasing the total numerical effort. The reason for this can be found in the large discrepancy of stiffness terms related to bending and membrane deformations, respectively. In thin shells, the membrane stiffness is, in relation to the bending stiffness, very high. As a result, small and moderate approximation errors in the incremental update of the displacements lead to very high residuals in the terms related to membrane forces, which can lead to divergence of the Newton scheme. This problem does not exist in mixed formulations, where stresses or stress resultants (including membrane forces) are treated as independent variables. However, mixed formulations come at the cost of additional variables to be discretized and solved for, and specific requirements on the discretization spaces of the different variables [37,38]. The goal of the MIP approach is to combine the simplicity and efficiency of displacement-based formulations with the improved robustness in the iterative scheme of mixed formulations. To this end, additional variables are introduced for stresses or stress resultants, similar to mixed methods. Unlike classical mixed methods, these variables are not assumed continuous and are not discretized, but are defined as local variables at each integration point. Due to this local definition, they can be eliminated from the formulation analytically by static condensation of the equation system, such that only displacement variables are discretized and solved for, like in a standard displacement-based formulation. As a matter of fact, an MIP formulation can be considered as a modified Newton method for a standard displacement formulation.

In this section, we apply this approach to the hyperelastic Kirchhoff–Love shell formulation presented in the previous section. The approach presented in the following can be considered as a general procedure of applying the MIP concept to nonlinear problems. First, we enhance the solution and residual vectors for the newly introduced variables and related equations accordingly, then we consistently linearize the enhanced residual equation resulting in an enhanced tangential stiffness matrix, and finally, we perform static condensation to eliminate the additional variables and reduce the equation system to its original size with displacement degrees of freedom as the only solution variables.

At each integration point, we introduce the independent variables $\tilde{\mathbf{n}}_i$ and $\tilde{\mathbf{m}}_i$, for membrane forces and bending moments, respectively. For a consistent notation, all following variables depending on these newly introduced variables will be indicated with a $\tilde{()}$ symbol. As in (45), we gather these stress resultants in a generalized stress resultant vector

$$\tilde{\mathbf{t}}_i = \begin{pmatrix} \tilde{\mathbf{n}}_i \\ \tilde{\mathbf{m}}_i \end{pmatrix} , \tag{57}$$

and obtain the corresponding related quantities as in (50)–(56)

$$\tilde{\mathbf{F}}^{int} = \sum_{i=1}^{N_s} \mathbf{B}_i^T \tilde{\mathbf{t}}_i \, w_i , \tag{58}$$

$$\tilde{\mathbf{R}} = \tilde{\mathbf{F}}^{int} - \mathbf{F}^{ext} , \tag{59}$$

$$\tilde{\mathbf{K}}^{geo} = \sum_{i=1}^{N_s} \tilde{\mathbf{k}}_i^{geo} \, w_i , \tag{60}$$

$$\tilde{k}_{rsi}^{geo} = \tilde{\mathbf{t}}_i^T \boldsymbol{\rho}_{,rsi} \ . \tag{61}$$

For ensuring equilibrium, we add an additional equation at each integration point

$$\tilde{\mathbf{s}}_i = \tilde{\mathbf{t}}_i - \mathbf{t}_i \ . \tag{62}$$

where $\tilde{\mathbf{s}}_i$ is a local residual, which should vanish at the end of each iteration. We can gather these local variables and local residuals in global vectors $\tilde{\mathbf{T}}$ and $\tilde{\mathbf{S}}$

$$\tilde{\mathbf{T}} = \begin{pmatrix} \tilde{\mathbf{t}}_1 \\ \tilde{\mathbf{t}}_2 \\ \dots \\ \tilde{\mathbf{t}}_{N_s} \end{pmatrix} , \qquad \tilde{\mathbf{S}} = \begin{pmatrix} \tilde{\mathbf{s}}_1 \\ \tilde{\mathbf{s}}_2 \\ \dots \\ \tilde{\mathbf{s}}_{N_s} \end{pmatrix} , \tag{63}$$

and then define the total vector of unknowns $\tilde{\mathbf{u}}_t$ and the total residual $\tilde{\mathbf{R}}_t$ as

$$\tilde{\mathbf{u}}_t = \begin{pmatrix} \tilde{\mathbf{T}} \\ \mathbf{u} \end{pmatrix} , \qquad \tilde{\mathbf{R}}_t = \begin{pmatrix} \tilde{\mathbf{S}} \\ \tilde{\mathbf{R}} \end{pmatrix} . \tag{64}$$

The residual equation system $\tilde{\mathbf{R}}_t = \mathbf{0}$ is linearized with respect to $\tilde{\mathbf{u}}_t$

$$\tilde{\mathbf{R}}_t + \frac{\mathrm{d}\tilde{\mathbf{R}}_t}{\mathrm{d}\tilde{\mathbf{u}}_t}\dot{\tilde{\mathbf{u}}}_t = \mathbf{0} , \tag{65}$$

which can be expressed block-wise as

$$\begin{pmatrix} \frac{\mathrm{d}\tilde{\mathbf{S}}}{\mathrm{d}\tilde{\mathbf{T}}} & \frac{\mathrm{d}\tilde{\mathbf{S}}}{\mathrm{d}\mathbf{u}} \\ \frac{\mathrm{d}\tilde{\mathbf{R}}}{\mathrm{d}\tilde{\mathbf{T}}} & \frac{\mathrm{d}\tilde{\mathbf{R}}}{\mathrm{d}\mathbf{u}} \end{pmatrix} \begin{pmatrix} \dot{\tilde{\mathbf{T}}} \\ \dot{\mathbf{u}} \end{pmatrix} = - \begin{pmatrix} \tilde{\mathbf{S}} \\ \tilde{\mathbf{R}} \end{pmatrix} , \tag{66}$$

or, more explicitly

$$\begin{pmatrix} \mathbf{1} & \mathbf{0} & \cdots & \cdots & -\mathbf{D}_1\mathbf{B}_1 \\ \mathbf{0} & \mathbf{1} & \cdots & \cdots & -\mathbf{D}_2\mathbf{B}_2 \\ \vdots & \vdots & \ddots & \vdots & \vdots \\ \vdots & \vdots & \cdots & \mathbf{1} & -\mathbf{D}_{N_s}\mathbf{B}_{N_s} \\ \mathbf{B}_1^T w_1 & \mathbf{B}_2^T w_2 & \cdots & \mathbf{B}_{N_s}^T w_{N_s} & \tilde{\mathbf{K}}^{geo} \end{pmatrix} \begin{pmatrix} \dot{\tilde{\mathbf{t}}}_1 \\ \dot{\tilde{\mathbf{t}}}_2 \\ \vdots \\ \dot{\tilde{\mathbf{t}}}_{N_s} \\ \dot{\mathbf{u}} \end{pmatrix} = - \begin{pmatrix} \mathbf{s}_1 \\ \mathbf{s}_2 \\ \vdots \\ \mathbf{s}_{N_s} \\ \tilde{\mathbf{R}} \end{pmatrix} . \tag{67}$$

As can be seen, the equations for the updates of the stress variables $\dot{\tilde{\mathbf{t}}}_i$ are independent of each other, which is due to the fact that they are defined locally at each integration point. As a consequence, these variables can be statically condensed from the equation system by formally solving for $\dot{\tilde{\mathbf{t}}}_i$

$$\dot{\tilde{\mathbf{t}}}_i = \mathbf{D}_i\mathbf{B}_i\dot{\mathbf{u}} - \tilde{\mathbf{s}}_i , \tag{68}$$

and substituting it back into (67), yielding the condensed equation system

$$\tilde{\mathbf{K}}_c\dot{\mathbf{u}} = \tilde{\mathbf{R}}_c , \tag{69}$$

with

$$\tilde{\mathbf{K}}_c = \sum_{i=1}^{N_s} \left(\mathbf{B}_i^T\mathbf{D}_i\mathbf{B}_i + \tilde{\mathbf{k}}_i^{geo} \right) w_i \tag{70}$$

for the condensed tangential stiffness matrix. The condensed residual vector is given by

$$\tilde{\mathbf{R}}_c = \tilde{\mathbf{F}}_c^{int} - \mathbf{F}^{ext} = \mathbf{R} , \tag{71}$$

since

$$\tilde{\mathbf{F}}_c^{int} = \sum_{i=1}^{N_s} \left(\mathbf{B}_i^T\tilde{\mathbf{t}}_i - \mathbf{B}_i^T\mathbf{s}_i \right) w_i = \sum_{i=1}^{N_s} \left(\mathbf{B}_i^T\tilde{\mathbf{t}}_i - \mathbf{B}_i^T \left(\tilde{\mathbf{t}}_i - \mathbf{t}_i \right) \right) w_i \tag{72}$$

$$= \sum_{i=1}^{N_s} \left(\mathbf{B}_i^T\mathbf{t}_i \right) w_i = \mathbf{F}^{int} . \tag{73}$$

As can be seen, the condensed vector of internal forces and, therefore, the condensed residual vector of the MIP formulation are identical to those of the standard displacement-based formulation. This is a typical feature of the MIP approach and it guarantees that the solution of the MIP formulation (in each load step) is identical to the one of the standard displacement-based solution. Only the tangential stiffness matrix, more precisely, the geometric stiffness matrix, is modified by the locally defined mixed variables. These are updated in each iteration according to

$$\dot{\tilde{\mathbf{t}}}_i = \mathbf{D}_i\mathbf{B}_i\dot{\mathbf{u}} - \tilde{\mathbf{s}}_i . \tag{74}$$

Table 1
Schematic description of the principal points of the algorithms: the differences between the standard and the MIP Newton's methods are marked in red. Δ indicates the extrapolation values from the kth (converged) step at the beginning of the new iteration loop j.

	Newton	MIP Newton
Predictor	$\mathbf{u}^1 = \mathbf{u}_{(k)} + \Delta\mathbf{u}$ $\mathbf{F}^{ext\,1} = \mathbf{F}^{ext}_{(k)} + \Delta\mathbf{F}^{ext}$ $\mathbf{t}_i^1 = \mathbf{t}_i(\mathbf{u}^1)$	$\mathbf{u}^1 = \mathbf{u}_{(k)} + \Delta\mathbf{u}$ $\mathbf{F}^{ext\,1} = \mathbf{F}^{ext}_{(k)} + \Delta\mathbf{F}^{ext}$ $\tilde{\mathbf{t}}_i^1 = \tilde{\mathbf{t}}_{i(k)} + \dot{\tilde{\mathbf{t}}}_i$
Iteration matrix	$\mathbf{K}(\mathbf{t}_i(\mathbf{u}^j), \mathbf{u}^j)$	$\mathbf{K}(\tilde{\mathbf{t}}_i^j, \mathbf{u}^j)$
Residual vector	$\mathbf{F}_c^{extj} - \mathbf{F}^{intj}$	$\mathbf{F}_c^{extj} - \mathbf{F}^{intj}$
New estimate	$\mathbf{u}^{j+1} = \mathbf{u}^j + \dot{\mathbf{u}}$ $\mathbf{F}^{ext(j+1)} = \mathbf{F}^{extj} + \dot{\mathbf{F}}^{ext}$ $\mathbf{t}_i^{j+1} = \mathbf{t}_i(\mathbf{u}^{j+1})\tilde{\mathbf{t}}$	$\mathbf{u}^{j+1} = \mathbf{u}^j + \dot{\mathbf{u}}$ $\mathbf{F}^{ext(j+1)} = \mathbf{F}^{extj} + \dot{\mathbf{F}}^{ext}$ $\tilde{\mathbf{t}}_i^{j+1} = \tilde{\mathbf{t}}_i^j + \dot{\tilde{\mathbf{t}}}_i$

We note that the MIP-based iterative scheme is very simple to implement and few changes with respect to a standard displacement-based Newton procedure are required (see Table 1). The MIP concept has been extensively and successfully tested for geometrically nonlinear problems [12,30] and has been extended to material nonlinearity here. We highlight that the consistent derivation presented in this section is general, it is not restricted to the specific shell formulation or hyperelastic materials, but can be applied to arbitrary nonlinear problems.

4. Iterative solution for the one-step energy-conserving method in displacement and mixed form

In this section, the general MIP approach presented above is extended to the one-step energy-conserving time integration method proposed in [31], which we refer to for deepening the argument. Here the equations are briefly recalled in order to present a unified updating process for the mixed variables involved in the iterative algorithm. Applying a spatial discretization and following the assembly process as described above, the semi-discrete global set of equations of motion can be written, leaving out the damping term, as

$$\begin{cases} \mathbf{v} = \mathbf{u}_{,t} \\ \mathbf{M}\mathbf{v}_{,t} + \mathbf{F}^{int}(\mathbf{u}) = \mathbf{F}^{ext} \end{cases} \tag{75}$$

where $\mathbf{M}$ is the mass matrix and where $(\cdot)_{,t}$ denotes a time derivative while $\mathbf{v}$ is the velocity vector. In one-step time integration schemes, $\alpha = \dfrac{t - t_0}{t_1 - t_0}$ is introduced to obtain the approximation in time for $\mathbf{u}$ and $\mathbf{v}$ over the time step $[t_0, t_1]$ with $t_1 = t_0 + \Delta t$:

$$\begin{cases} \mathbf{v}(\alpha) = \mathbf{v}_0 + \alpha(\mathbf{v}_1 - \mathbf{v}_0) \\ \mathbf{u}(\alpha) = \mathbf{u}_0 + \alpha(\mathbf{u}_1 - \mathbf{u}_0) \ . \end{cases} \tag{76}$$

A possible choice to rewrite in discrete form the semi-discrete equations of motion (75) is

$$\begin{cases} \bar{\mathbf{v}} = \dfrac{\mathbf{u}_1 - \mathbf{u}_0}{\Delta t} \\ \mathbf{M}\dfrac{\mathbf{v}_1 - \mathbf{v}_0}{\Delta t} + \bar{\mathbf{F}}^{int}(\mathbf{u}) = \bar{\mathbf{F}} \end{cases} \tag{77}$$

where $\bar{\mathbf{v}}$, $\bar{\mathbf{F}}^{int}$ and $\bar{\mathbf{F}}^{ext}$ are the mean values of $\mathbf{v}(\alpha)$, $\mathbf{F}^{int}(\alpha)$ and $\mathbf{F}^{ext}(\alpha)$ over the step

$$\begin{cases} \dfrac{\mathbf{v}_1 + \mathbf{v}_0}{2} = \dfrac{\mathbf{u}_1 - \mathbf{u}_0}{\Delta t} \\ \mathbf{M}\dfrac{\mathbf{v}_1 - \mathbf{v}_0}{\Delta t} + \bar{\mathbf{F}}^{int}(\mathbf{u}) = \bar{\mathbf{F}}^{ext} \quad \text{with} \quad \bar{\mathbf{F}}^{ext} \equiv \displaystyle\int_0^1 \mathbf{F}^{ext}(\alpha) d\alpha \ . \end{cases} \tag{78}$$

The iterative Newton-like solution method for the time integration proposed in [31] operates over the end-step displacement $\mathbf{u}_1$ as unknown. The residual discrete equations of motion $\mathbf{F}_1^{int} = \mathbf{F}^{int}(\mathbf{u}_1)$ are

$$\mathbf{R}_1 \equiv 2\mathbf{M}\frac{\mathbf{u}_1 - \mathbf{u}_0 - \mathbf{v}_0\Delta t}{\Delta t^2} + \bar{\mathbf{F}}_1^{int} - \bar{\mathbf{F}}^{ext} = \mathbf{0} \ . \tag{79}$$

The mean internal force vector $\bar{\mathbf{R}}_1 = \bar{\mathbf{R}}(\mathbf{u}_1)$, introduced in (79), is defined as sum of spatial integration point contributions

$$\bar{\mathbf{F}}_1^{int} = \sum_{i=1}^{N_s} \bar{\mathbf{B}}_i^T \mathbf{t}_i w_i \quad \text{with} \quad \mathbf{t}_i(\mathbf{u}_1) = \mathbf{t}_i \left(\frac{\boldsymbol{\rho}_i(\mathbf{u}_1) + \boldsymbol{\rho}_i(\mathbf{u}_0)}{2} \right) \tag{80}$$

while the tangent stiffness matrix $\bar{\mathbf{K}}_1 = \bar{\mathbf{K}}(\mathbf{u}_1)$ is

$$\bar{\mathbf{K}}_1 \equiv \frac{\partial \bar{\mathbf{F}}_1^{int}}{\partial \mathbf{u}_1} = \sum_{i=1}^{N_s} \left(\bar{\mathbf{B}}_i^T \mathbf{D}_i \mathbf{B}_i w_i + \bar{\mathbf{k}}_i^{geo} \right) \tag{81}$$

where $\bar{\mathbf{B}}_i(\mathbf{u}_1)$ and $\bar{\mathbf{k}}_i^{geo}(\mathbf{u}_1)$ are the mean contribution to the residual and to the geometrical stiffness evaluated as a sum over temporal integration points defined by coordinates α_n and weights ϖ_n

$$\bar{\mathbf{B}}_i \equiv \sum_{n=1}^{N_t} \mathbf{B}_i(\mathbf{u}(\alpha_n))\varpi_n, \;\; \bar{\mathbf{k}}_i^{geo} \equiv \sum_{n=1}^{N_t} \mathbf{k}_i^{geo}(\mathbf{u}(\alpha_n), \mathbf{t}_1), \varpi_n \; .$$

It is the case to note that the elastic stress $\mathbf{t}_i$ in (80) cannot be evaluated through the deformation tensor evaluated using the displacement field as in [25]. It is evident that the displacement corresponding to the average strain is not available within the analysis and then it must be evaluated using (21). The rule for the displacement update based on Newton iteration is then

$$\mathbf{u}_1^{j+1} = \mathbf{u}_1^j - \left[\frac{2}{\Delta t^2} \mathbf{M} + \bar{\mathbf{K}}_1^j \right]^{-1} \mathbf{R}_1^j \; . \tag{82}$$

In applying the MIP concept, as usual, at each iteration loop, the constitutive relations are relaxed and solved together with the motion equations as a parallel set of equations, so that

$$\tilde{\bar{\mathbf{F}}}^{int}(\tilde{\mathbf{t}}, \mathbf{u}_1) = \sum_{i=1}^{N_s} \bar{\mathbf{B}}_i^T \tilde{\mathbf{t}}_i w_i$$

with, again, $\tilde{\mathbf{t}}_i$ independent variables. Similarly to (62), the extended system of equations is

$$\begin{cases} \tilde{\mathbf{s}}_i(\tilde{\mathbf{t}}_i, \mathbf{u}_1) \equiv \tilde{\mathbf{t}}_i - \mathbf{t}_1 = \mathbf{0} \\ \tilde{\mathbf{R}}(\tilde{\mathbf{t}}, \mathbf{u}_1) \equiv 2\mathbf{M} \dfrac{\mathbf{u}_1 - \mathbf{u}_0 - \mathbf{v}_0 \Delta t}{\Delta t^2} + \tilde{\bar{\mathbf{F}}}^{int}(\tilde{\mathbf{t}}, \mathbf{u}_1) - \bar{\mathbf{F}}^{ext} = \mathbf{0} \; . \end{cases} \tag{83}$$

The resulting iteration scheme, including the stress updates, is:

$$\begin{cases} \mathbf{u}_1^{j+1} = \mathbf{u}_1^j - \left[\dfrac{2}{\Delta t^2} \mathbf{M} + \tilde{\bar{\mathbf{K}}}(\tilde{\mathbf{t}}^j, \mathbf{u}_1^j) \right]^{-1} \tilde{\mathbf{R}}^j \\ \tilde{\mathbf{t}}_i^{j+1} = \tilde{\mathbf{t}}_i^j - \mathbf{s}_i^j + \mathbf{D}_i \mathbf{B}_i^j (\mathbf{u}_1^{j+1} - \mathbf{u}_1^j) \end{cases} \tag{84}$$

with $\tilde{\bar{\mathbf{K}}}(\tilde{\mathbf{t}}^j, \mathbf{u}_1^j)$ that has the same expression as in Eq. (81) but evaluated using the independent $\tilde{\mathbf{t}}_i^j$ instead of its counterpart coming from $\mathbf{u}_1^j$. As previously observed the internal force vector must be the same in both MIP and displacement formulation and the correction of the generalized stress is of the same shape as the static nonlinear case

$$\tilde{\mathbf{t}}_i^{j+1} = \mathbf{t}_i^j + \mathbf{D}_i \mathbf{B}_i^j (\mathbf{u}_1^{j+1} - \mathbf{u}_1^j) \; .$$

As implementation insight, it is the case to note that if the new stress value is expressed in terms of increment $\tilde{\mathbf{t}}_i^{j+1} = \tilde{\mathbf{t}}_i^j + \dot{\tilde{\mathbf{t}}}_i$ the correction stress update is formally equal to the (74).

5. Numerical results

In this section, we present some benchmarks devoted to checking both the correctness of the proposed simplified model (KLS) defined in (12) in the context of hyperelastic materials and the effect of MIP [9] on the iteration process.

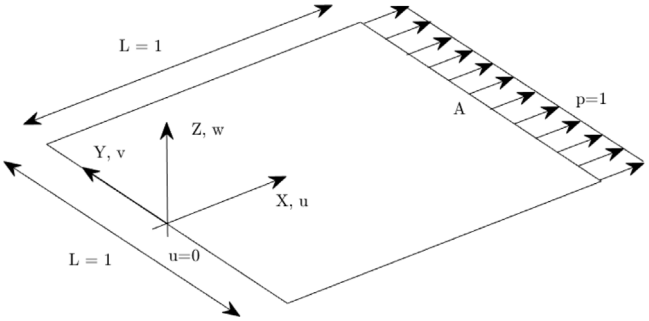

Fig. 1. Tensile test: problem setup.

Table 2
Tensile test: Cumulative iteration numbers of the MIP and displacement-based (D) formulations under load-control, for different neo-Hookean materials.

Model	$\nu = 0.49$	$\nu = 0.499$	inc
D	60	54	54
MIP	59	55	55

5.1. Tensile test

The simple uniaxial tensile test has been studied in [25] where the comparison with analytical solutions was presented for different constitutive laws. The square membrane, see Fig. 1, of unit length and thickness $h = 0.01$ is supported on one edge (at $x = 0$) in x-direction and subjected to uniaxial unit tensile loading at the opposite edge. The domain is modeled using a single cubic element, and boundary conditions in y and z are applied such that rigid body motions are prevented. We consider compressible and incompressible neo-Hookean and Mooney–Rivlin material models [39–41], with

$$\psi_{el}^{nh} = \frac{1}{2}\mu\,(I_1 - 3)\,, \tag{85}$$

$$\psi_{el}^{mr} = \frac{1}{2}\mu_1\,(I_1 - 3) - \frac{1}{2}\mu_2\,(I_2 - 3) \tag{86}$$

describing the incompressible neo-Hookean (85) and Mooney–Rivlin (86) materials, and

$$\psi^{nh} = \frac{1}{2}\mu\left(J^{-2/3}I_1 - 3\right) + \frac{1}{4}K\left(J^2 - 1 - 2\ln J\right), \tag{87}$$

$$\psi^{mr} = \frac{1}{2}\mu_1\left(J^{-2/3}I_1 - 3\right) - \frac{1}{2}\mu_2\left(J^{-4/3}I_2 - 3\right) + \frac{1}{4}K\left(J^2 - 1 - 2\ln J\right) \tag{88}$$

describing the compressible neo-Hookean (87) and Mooney–Rivlin (88) materials. In (85)–(88), μ is the shear modulus, K the bulk modulus, and I_i denote the invariants of the deformation tensor, defined by $I_1 = \mathrm{tr}(\mathbf{C})$, $I_2 = \frac{1}{2}\left(\mathrm{tr}(\mathbf{C})^2 - \mathrm{tr}(\mathbf{C}^2)\right)$, $I_3 = \det(\mathbf{C})$ [41]. The material parameters are chosen as $\mu = 1.5\ 10^6$ for the shear modulus and $\mu_1 = 0.875\mu$, and $\mu_2 = -0.125\mu$. In the compressible cases, different values for the Poisson's ratio $\nu = \{0.45, 0.49, 0.499\}$ are considered, defining the bulk modulus via $K = 2\mu(1+\nu)/(3-6\nu)$. The thickness change factor λ_3 can be evaluated using $\lambda_3 = \sqrt{C_{33}}$ and is also tested in the numerical experiments.

In Table 2 the performance of MIP and displacement-based (D) formulations are compared in terms of Newton iterations.

As it is expected by the discussion given in [9,18] the MIP and the displacement-based formulation perform similarly as only the membrane stiffness is mobilized.

Figs. 2 and 3 show the $\lambda_3 - \lambda$ and $u_A - \lambda$ curves for compressible and incompressible Neo-Hookean materials. The solutions for compressible and incompressible Mooney–Rivlin materials are shown in Figs. 4 and 5. In all cases, the curves show a perfect match of the full and the simplified KL shell models.

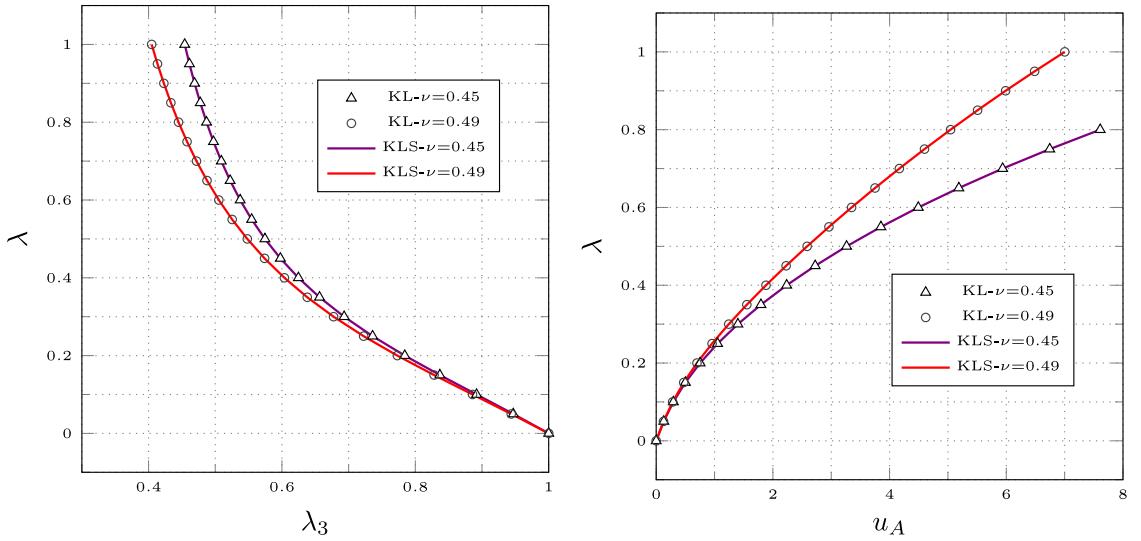

Fig. 2. Tensile test: Thickness change factor λ_3 and load–displacement λ-u_A for a compressible neo-Hookean material with different Poisson's ratios. Comparison of the full Kirchoff–Love model (KL) and the simplified model (KLS).

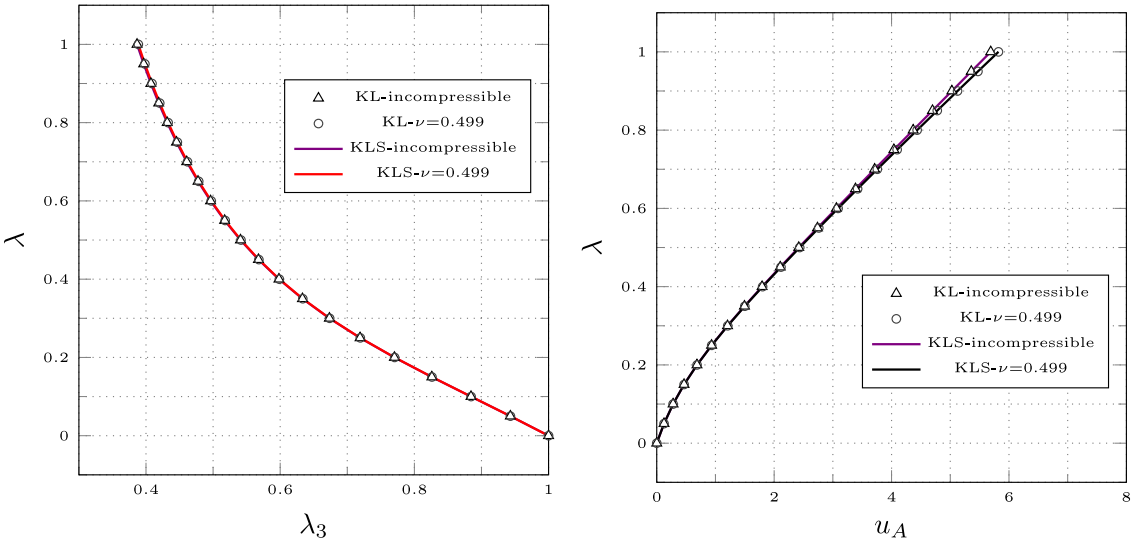

Fig. 3. Tensile test: Thickness change factor λ_3 and load–displacement λ-u_A for incompressible and nearly incompressible neo-Hookean materials.

5.2. *Inflation of a balloon*

In this benchmark problem, the inflation of a balloon is modeled. The balloon is modeled by a sphere with an initial radius $R = 10$ and $h = 0.1$ of which 1/8th of the surface is modeled using 4×4 cubic elements, as depicted in Fig. 6. The balloon is subjected to an internal pressure. An analytical solution is given in [41] for an incompressible neo-Hookean (85) and an incompressible Mooney–Rivlin (86) material, and the problem was solved successfully with the KL shell model in [25], which herein is used to validate the KLS proposed in the present paper. As material property we choose $\mu = 4.225 \cdot 10^5$, $\mu_1 = 0.875\mu$, and $\mu_2 = -0.125\mu$.

In Fig. 7 the highlighted part (in gray) is the deformed shape obtained with the full model, the white part is obtained by the simplified one, and the green part is the undeformed geometry. As it is possible to observe the portions match perfectly. In the comparison of neo-Hookean and Mooney–Rivlin constitutive models, the same

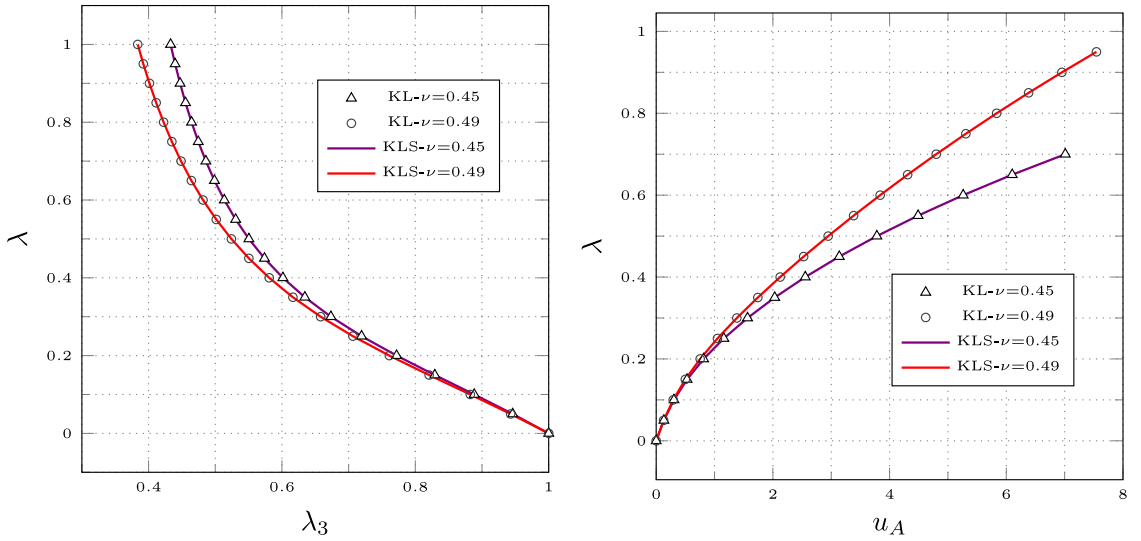

Fig. 4. Tensile test: Thickness change factor λ_3 and displacement u_A for different Mooney–Rivlin materials.

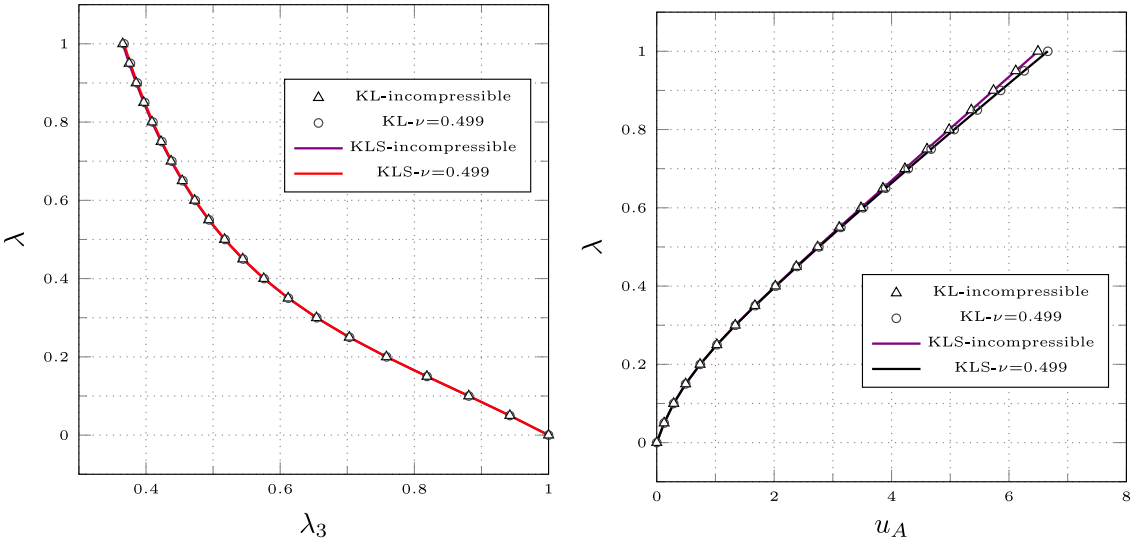

Fig. 5. Tensile test: Thickness change factor λ_3 and displacement u_A for incompressible and nearly incompressible Mooney–Rivlin materials.

scaling of the axes has been used. For both materials the $\lambda_1 - \lambda$ and $u_A - \lambda$ curves show the ability of the simplified model to describe the same solution of the full model as it is shown in Figs. 8 and 9. The equilibrium paths are drawn by evaluating the actual pressure as $p = \frac{\lambda}{A}$, and the membrane stretches as $\lambda_1 = \lambda_2 = \sqrt{\frac{A}{A_0}}$ where A_0 and A are the initial and the actual surface area, respectively.

5.3. Cantilever beam

As a first bending-dominated problem, we propose the cantilever beam shown in Fig. 10. In this case, the effect of the MIP formulation is expected to be relevant. The beam is modeled as a rectangular 10.0 × 1.0 shell with thickness $h = 0.10$ ($L/h = 100$) and loaded with a unit line load at the free edge. Compressible and incompressible neo-Hookean materials with the same material properties as in the tensile test of Section 5.1 are used. A mesh of 8 × 1 cubic elements is used. Finally, it is the case to note that membrane locking is cured by using the reduced

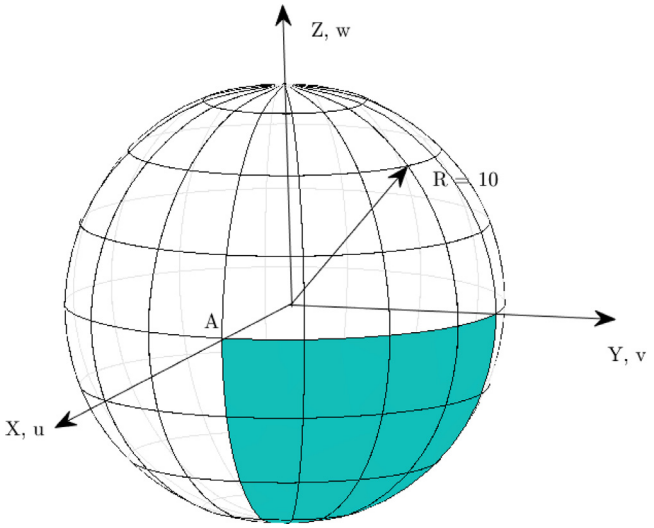

Fig. 6. Initial geometry of the inflation of a balloon benchmark. One eighth of a sphere with modeled with 4 × 4 cubic elements.

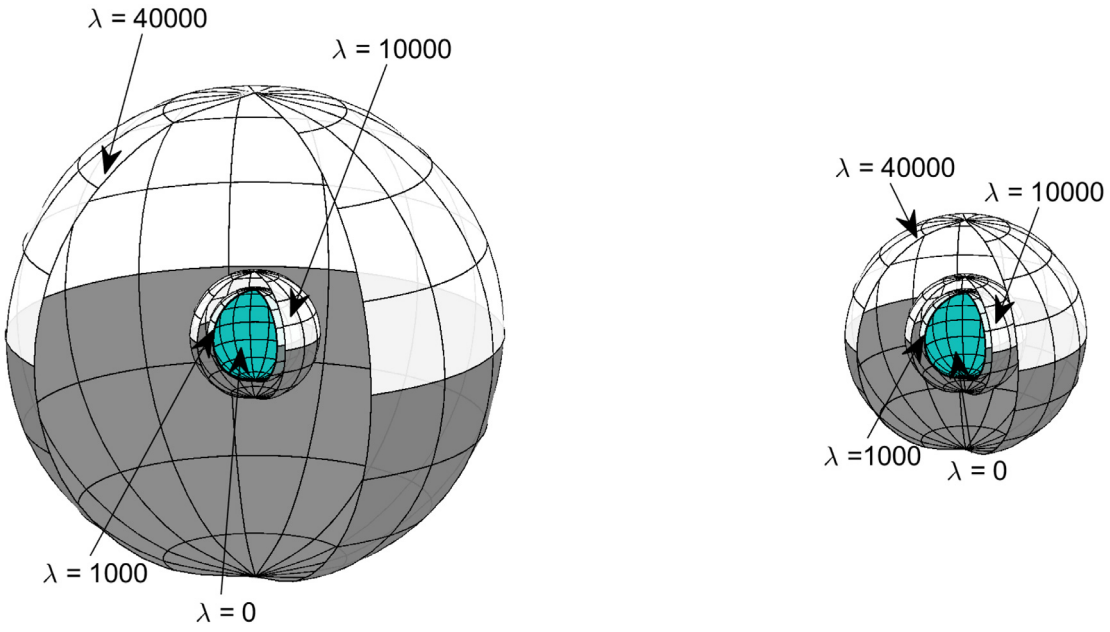

(a) neo-Hookean (b) Mooney-Rivlin

Fig. 7. Inflation of a balloon. Deformed shapes for different load levels.

integration scheme established in [30]. Table 3 shows the cumulative iterations required to execute the analysis with the displacement-based (D) and MIP formulations. It can be seen that the required iteration number with MIP is almost 50% of that required by the displacement-based solution process.

5.4. Pinched cylinder

This example regards the pinching of a cylinder. The cylinder has a radius $R = 9$, length $L = 30$, and thickness $h = 0.2$ and is subjected to line-loads on the top and bottom as shown in Fig. 11. Due to symmetry only a

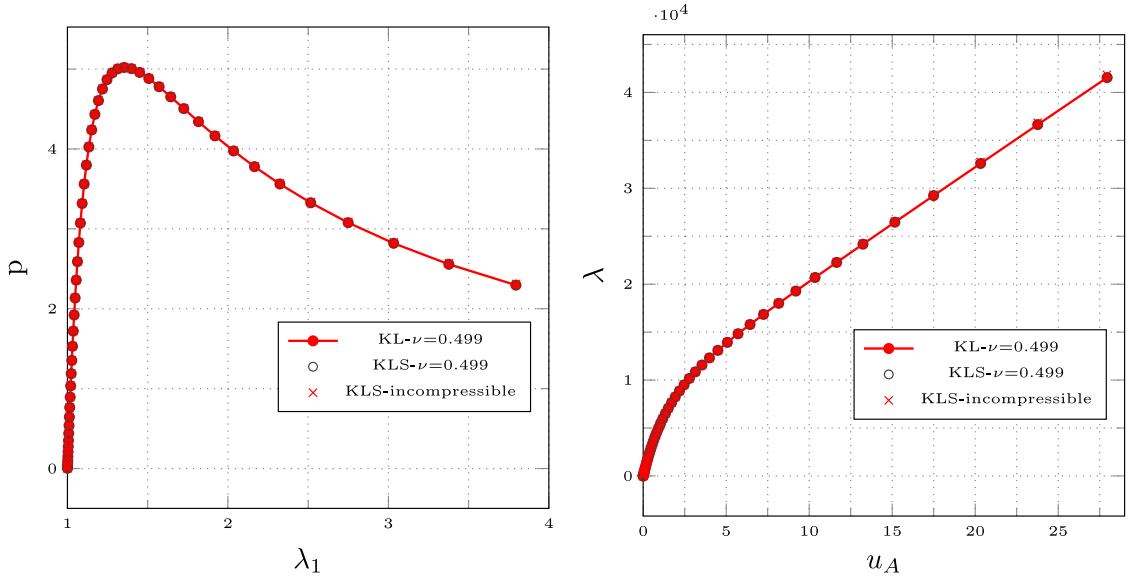

Fig. 8. Inflation of a balloon: comparison of simplified and full models for different neo-Hookean materials.

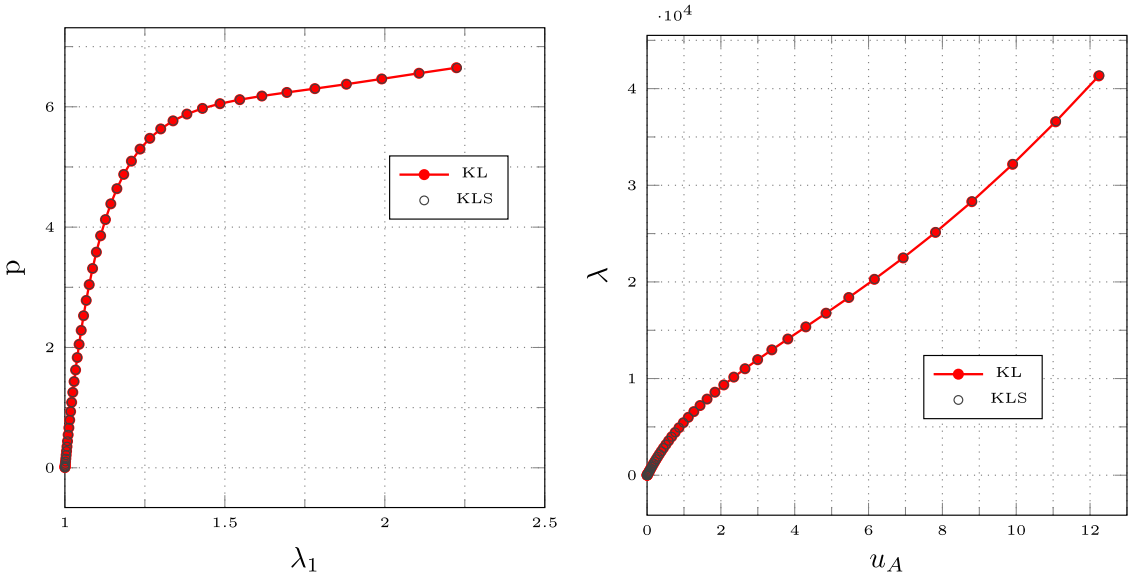

Fig. 9. Inflation of a balloon: comparison of simplified and full models for incompressible Mooney–Rivlin.

Table 3
Cantilever beam: total number of Newton iterations for different materials in nonlinear static case.

Model	$\nu = 0.45$	$\nu = 0.49$	$\nu = 0.499$	inc
D	64	63	63	63
MIP	30	30	30	30

quarter of the domain with symmetry conditions is modeled. The geometry is meshed by 8×16 cubic elements in radial and longitudinal directions, respectively. We analyze the load case of both inward and outward-directed loads. This problem setup is similar to the pinched cylinder problem originally proposed by [42] and also modeled

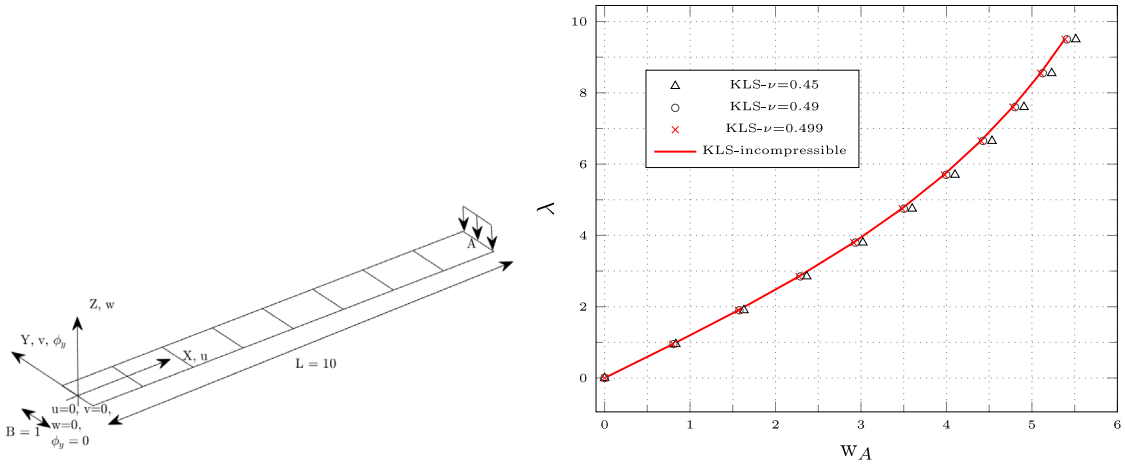

Fig. 10. Initial geometry of the cantilever beam (left). Load–displacement curve $\lambda - w_A$ for different neo-Hookean materials (right).

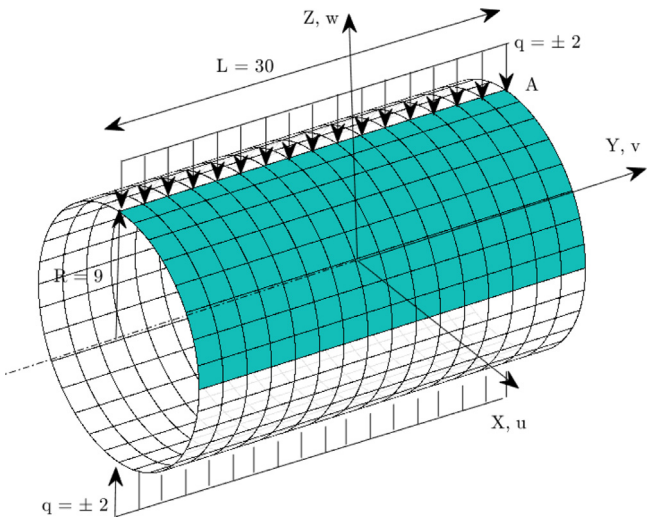

Fig. 11. The initial geometry of the cylinder for the pinched cylinder benchmark. The geometry is modeled by a quarter, as indicated, with symmetry conditions on both sides and with 8 elements in the radial direction and 16 in the length direction.

Table 4
Pinched cylinder: total number of Riks iterations for different load cases.

Model	Inward load	Outward load
D	100	48
MIP	63	31

in [25], which, however, has slightly different boundary conditions resulting in reduced symmetry, and considers inward-directed loads only. As in the original benchmark we use a compressible neo-Hookean material defined by the following strain energy function:

$$\Psi_{el} = \frac{\mu}{2}(I_1 - 3) - \mu \ln(\sqrt{I_3}) + \frac{\Lambda}{4}(I_3 - 1 - 2\ln(\sqrt{I_3})) \tag{89}$$

with $\mu = 60$ and $\Lambda = 240$ as the Lamé constants. Table 4 shows that the MIP improves the performances of the Newton method of almost 40% in this case for both inward load and of the 35% for the outward load case.

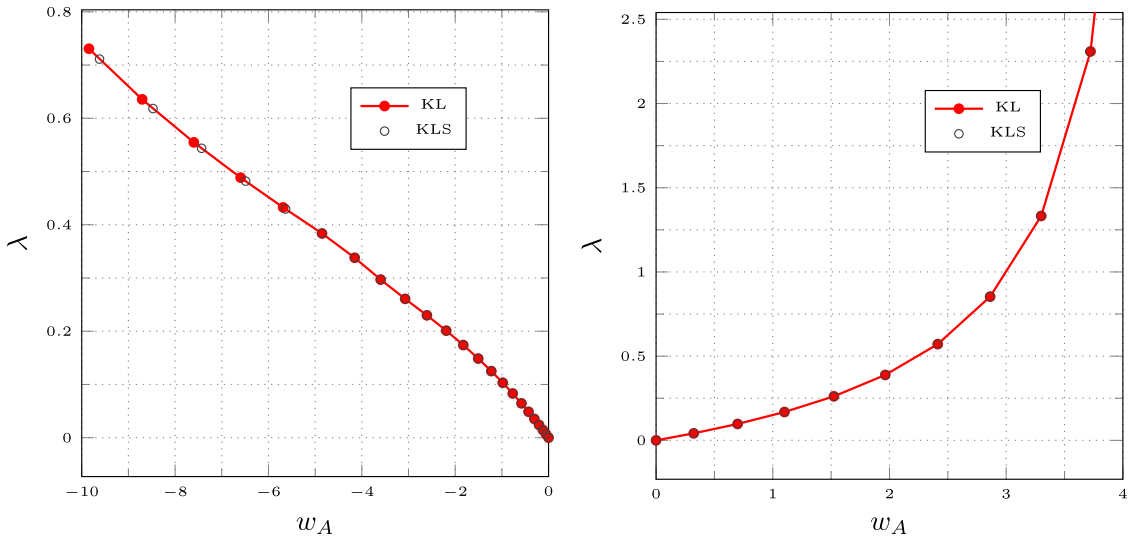

Fig. 12. Pinched cylinder: comparison of simplified and full models for neo-Hookean materials. Inward (left) and Outward (right) loads.

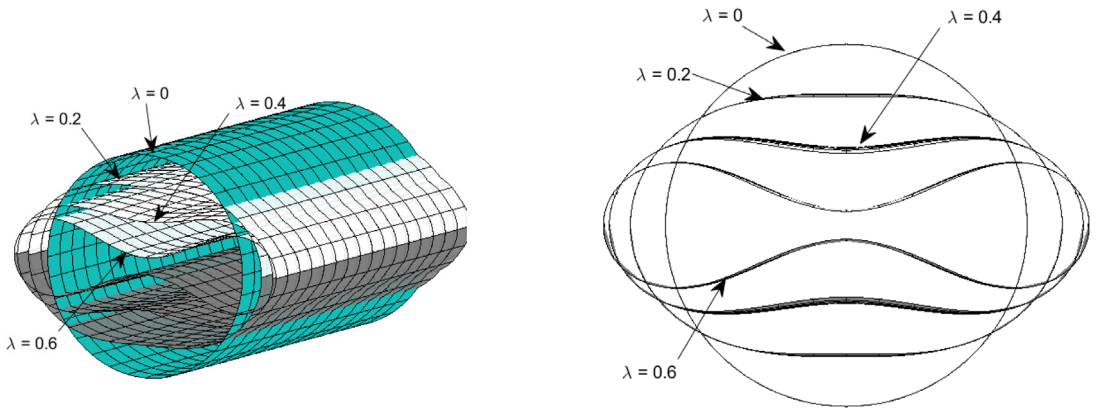

(a) 3D view

(b) X-Z plane view

Fig. 13. Pinched cylinder: Deformed shapes for different load levels and Inward load direction. (For interpretation of the references to color in this figure legend, the reader is referred to the web version of this article.)

Fig. 12 shows that the simplified and the full models overlap also in this case for both inward and outward load cases. Similarly to the case of the inflation of a balloon 5.2 the deformed shapes depicted in Figs. 13 and 14 are bicolor and compared with the undeformed geometry colored in green. Again, the gray parts represent the deformed shapes, for different load levels, obtained with the full model while the white part is obtained with the simplified one.

Furthermore, we use this example to give an indicative estimate on the computational saving by using the simplified bending strain measure based on the simplified formula for the normal vector (12) compared to a formulation with the consistent normal vector (2). For this comparison, the problem is solved with both formulations (simplified and standard bending strains) in a standard load-controlled Newton method. In this case, the total number of iterations is the same for both formulations, nevertheless, the formulation with the simplified bending strains results in a saving of almost 12% of the computation time.

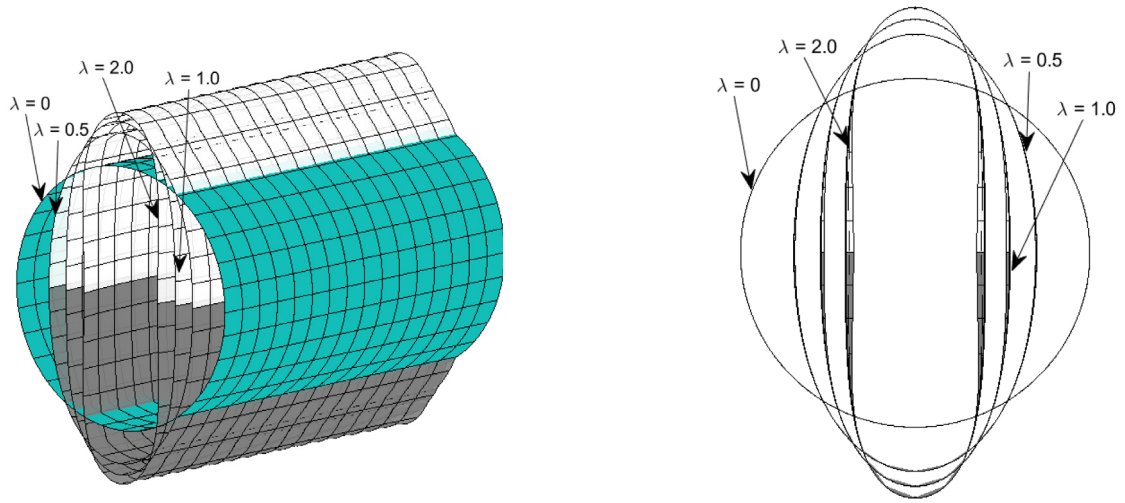

(a) 3D view (b) X-Z plane view

Fig. 14. Pinched cylinder: Deformed shapes for different load levels and Outward load direction. (For interpretation of the references to color in this figure legend, the reader is referred to the web version of this article.)

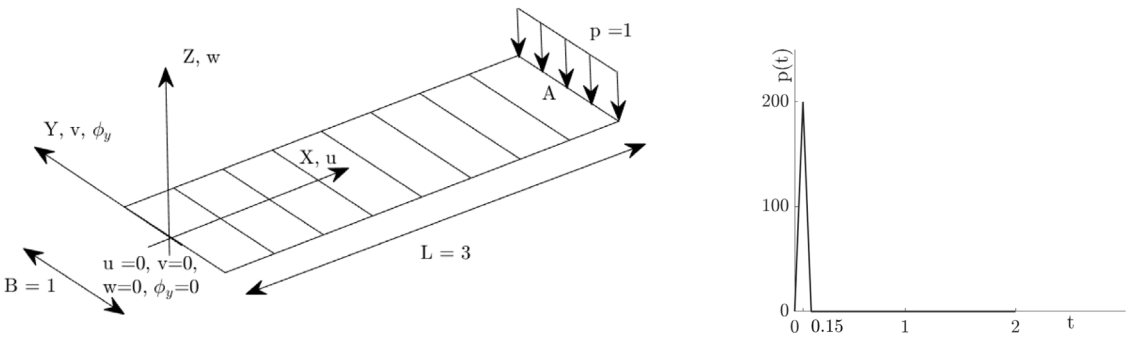

Fig. 15. Initial geometry of the vibrating beam.

5.5. Nonlinear dynamic benchmark problems

Within this section the method proposed in [31], considering three temporal integration points, is compared with the standard Newmark method [43]. For both examples, a compressible and incompressible neo-Hookean material with the same material property of the tensile test of Section 5.1 and 0.5 normalized mass density are used.

Firstly the cantilever beam, with thickness $h = 0.10$, is tested considering the loading law represented in Fig. 15. The Fig. 16 compares the performances of the mid-point rule method as proposed in [31] and the Newmark method [43] while Fig. 17 shows the ability of the model in well reproducing the behavior of nearly incompressible materials. It is possible to see that, also in the case of hyperelastic materials, the approach proposed in [31] is stable while the standard Newmark fails even for a very small step size.

Table 5 shows the cumulative iterations, total and average for time step (in brackets) when the mid-point rule [31] is executed for different Neo-Hookean materials. The MIP formulation allows us to save 12% (incompressible case) of the total number of iterations. If the time step Δt is halved we get, for the incompressible case, (D) 3705 (4.62) and (MIP) 3196 (3.99) respectively speeding up the solution process of the 15% and the solution process takes much more advantage from the mixed format.

A further test in the dynamical regime regards a square plate with thickness $h = 0.02$, meshed by 8×8 cubic elements, with one fixed edge, one simply supported and two free as depicted in Fig. 18. The dynamical response of the plate is reported in Fig. 19.

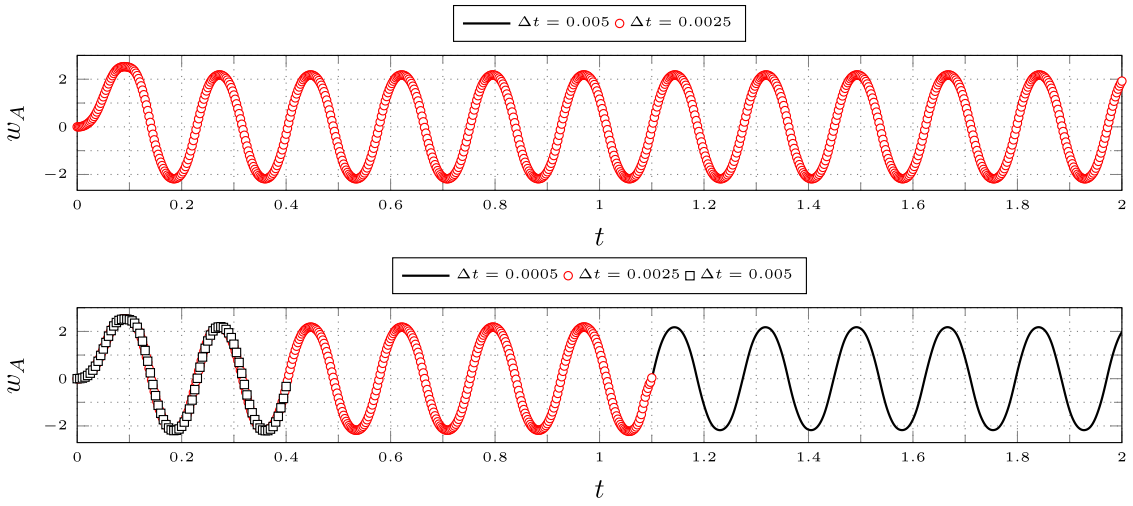

Fig. 16. Vibrating beam: $\nu = 0.45$ and different time step Δt. Comparison of the mid-point rule [31] (Top) and Newmak method (bottom).

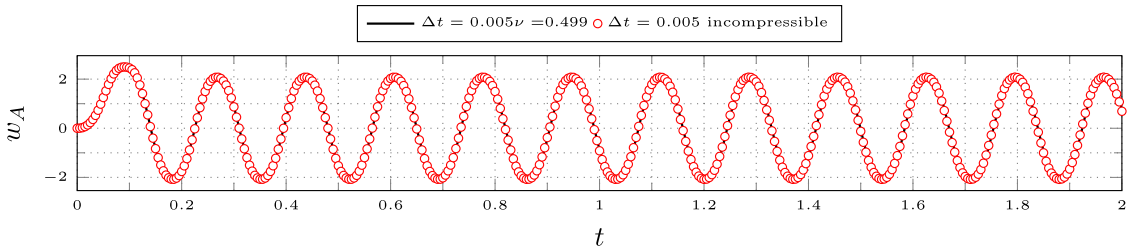

Fig. 17. Vibrating beam: mid-point rule. Incompressible vs. nearly incompressible.

Table 5
Vibrating beam: total number of Newton iterations (and average loops per time-step in brackets) for $\nu = 0.499$ and incompressible material and a time step $\Delta t = 0.005$. Results for the displacement-based (D) and MIP formulations.

Model	$\nu = 0.499$	inc
D	2264 (5.64)	2080 (5.19)
MIP	2047 (5.10)	1850 (4.61)

For this last example, the Newmark method (in both MIP and D formats) and the mid-point rule method [31] in the displacement (D) format have been also tested. In the former case, the time integration scheme diverges very soon while in the latter after 0.5 s the solver reports the warning for ill-conditioned iteration matrix. This example clearly shows that only the mid-point rule method [31] in MIP format is able to finish the analysis proving once more the robustness of the proposed approach.

6. Conclusions

We have presented a mixed integration point (MIP) formulation for structural problems including geometric and material nonlinearities. We have applied it to the case of hyperelastic Kirchhoff–Love shells with isogeometric discretization. However, the presented MIP formulation is general and can be applied to arbitrary structural formulations involving geometric and material nonlinearities. We have presented how to combine this formulation with a one-step energy-conserving time integration method [31] for extending the approach to structural dynamics. Moreover, we have tested the applicability of the simplified bending strain measure proposed for Kirchhoff–Love shells in the context of geometric nonlinearities [30] in the fully nonlinear regime including large strains. Several

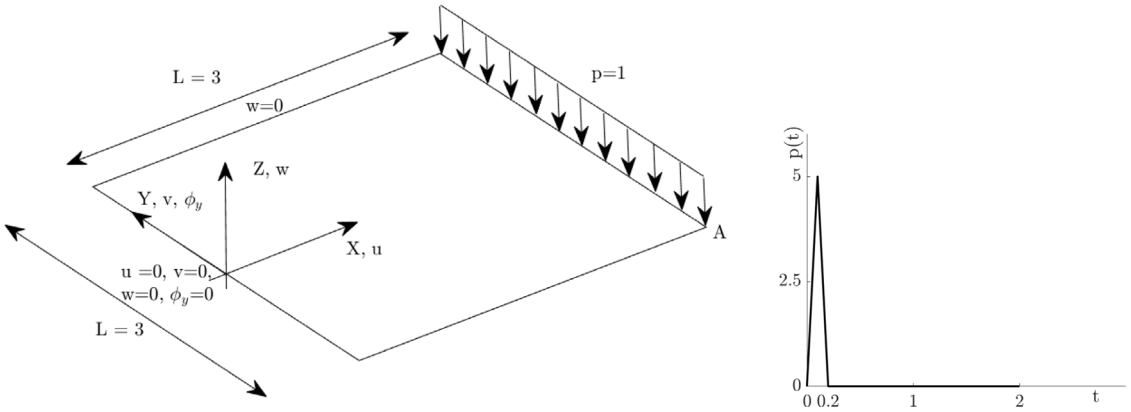

Fig. 18. Initial geometry of the vibrating plate.

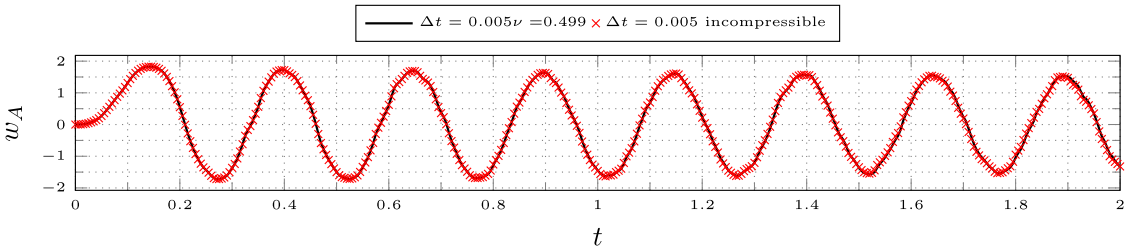

Fig. 19. Vibrating plate: mid-point rule MIP. Incompressible vs. nearly incompressible.

benchmark problems involving large deformations and large strains as well as statics and dynamics demonstrate the applicability and efficiency of the proposed formulations. Comparisons to a displacement-based formulation [25] showed that the MIP approach can significantly reduce the required number of Newton iterations in path-following methods for nonlinear static analysis as well as in implicit time integration schemes within nonlinear structural dynamics. Comparisons of the solutions obtained with the simplified bending strain measure [30] to those obtained with the full strain measure [44] showed that the simplified version also performs well in a large strain context, further improving the efficiency of the method.

Declaration of competing interest

The authors declare that they have no known competing financial interests or personal relationships that could have appeared to influence the work reported in this paper.

Data availability

No data was used for the research described in the article.

Acknowledgement

Josef Kiendl has received funding from the European Research Council (ERC) under the European Union's Horizon 2020 research and innovation program (grant agreement No 864482).

The authors are grateful to the DIMES department of the University of Calabria for having supported Prof. Josef Kiendl as visiting Professor within the MUR Departments of Excellence project (law 11 December 2016, n. 232).

References

[1] E. Riks, An incremental approach to the solution of snapping and buckling problems, Int. J. Solids Struct. 15 (7) (1979) 529–551, http://dx.doi.org/10.1016/0020-7683(79)90081-7.

[2] D.N. Arnold, Mixed finite element methods for elliptic problems, Comput. Methods Appl. Mech. Engrg. 82 (1–3) (1990) 281–300, http://dx.doi.org/10.1016/0045-7825(90)90168-L.
[3] M. Duan, An efficient hybrid/mixed element for geometrically nonlinear analysis of plate and shell structures, Comput. Mech. 35 (2004) 72–84.
[4] K. Sze, W. Chan, T. Pian, An eight-node hybrid-stress solid-shell element for geometric non-linear analysis of elastic shells, Internat. J. Numer. Methods Engrg. 55 (7) (2002) 853–878, http://dx.doi.org/10.1002/nme.535.
[5] S. Klinkel, F. Gruttmann, W. Wagner, A robust non-linear solid shell element based on a mixed variational formulation, Comput. Methods Appl. Mech. Engrg. 195 (1–3) (2006) 179–201, http://dx.doi.org/10.1016/j.cma.2005.01.013.
[6] T. Hughes, J.A. Cottrell, Y. Bazilevs, Isogeometric analysis: CAD, finite elements, NURBS, exact geometry and mesh refinement, Comput. Methods Appl. Mech. Engrg. 194 (39–41) (2005) 4135–4195, http://dx.doi.org/10.1016/j.cma.2004.10.008, http://linkinghub.elsevier.com/retrieve/pii/S0045782504005171, https://www.sciencedirect.com/science/article/pii/S0045782504005171#fig1.
[7] G. Sangalli, M. Tani, Matrix-free weighted quadrature for a computationally efficient isogeometric k-method, Comput. Methods Appl. Mech. Engrg. 338 (2018) 117–133, http://dx.doi.org/10.1016/j.cma.2018.04.029, URL http://www.sciencedirect.com/science/article/pii/S0045782518302081.
[8] K. Rafetseder, W. Zulehner, A new mixed approach to Kirchhoff–Love shells, Comput. Methods Appl. Mech. Engrg. 346 (2019) 440–455, http://dx.doi.org/10.1016/j.cma.2018.11.033, URL https://www.sciencedirect.com/science/article/pii/S0045782518305929.
[9] D. Magisano, L. Leonetti, G. Garcea, How to improve efficiency and robustness of the Newton method in geometrically non-linear structural problem discretized via displacement-based finite elements, Comput. Methods Appl. Mech. Engrg. 313 (2017) 986–1005, http://dx.doi.org/10.1016/j.cma.2016.
[10] L. Leonetti, F. Liguori, D. Magisano, G. Garcea, An efficient isogeometric solid-shell formulation for geometrically nonlinear analysis of elastic shells, Comput. Methods Appl. Mech. Engrg. 331 (2018) 159–183, http://dx.doi.org/10.1016/j.cma.2017.11.025, URL http://www.sciencedirect.com/science/article/pii/S0045782517307429.
[11] L.F. Leidinger, M. Breitenberger, A.M. Bauer, S. Hartmann, R. Wüchner, K.U. Bletzinger, F. Duddeck, L. Song, Explicit dynamic isogeometric B-Rep analysis of penalty-coupled trimmed NURBS shells, Comput. Methods Appl. Mech. Engrg. 351 (2019) 891–927, http://dx.doi.org/10.1016/j.cma.2019.04.016.
[12] L. Leonetti, F.S. Liguori, D. Magisano, J. Kiendl, A. Reali, G. Garcea, A robust penalty coupling of non-matching isogeometric Kirchhoff–Love shell patches in large deformations, Comput. Methods Appl. Mech. Engrg. 371 (2020) 113289, http://dx.doi.org/10.1016/j.cma.2020.113289, URL https://www.sciencedirect.com/science/article/pii/S0045782520304746.
[13] F.S. Liguori, D. Magisano, L. Leonetti, G. Garcea, Nonlinear thermoelastic analysis of shell structures: solid-shell modelling and high-performing continuation method, Compos. Struct. 266 (2021) 113734, http://dx.doi.org/10.1016/j.compstruct.2021.113734, URL https://www.sciencedirect.com/science/article/pii/S0263822321001951.
[14] F. Maurin, F. Greco, S. Dedoncker, W. Desmet, Isogeometric analysis for nonlinear planar Kirchhoff rods: Weighted residual formulation and collocation of the strong form, Comput. Methods Appl. Mech. Engrg. 340 (2018) 1023–1043, http://dx.doi.org/10.1016/j.cma.2018.05.025, URL http://www.sciencedirect.com/science/article/pii/S0045782518302706.
[15] F. Maurin, F. Greco, W. Desmet, Isogeometric analysis for nonlinear planar pantographic lattice: discrete and continuum models, Contin. Mech. Thermodyn. (2018) http://dx.doi.org/10.1007/s00161-018-0641-y.
[16] D. Magisano, L. Leonetti, G. Garcea, Isogeometric analysis of 3D beams for arbitrarily large rotations: Locking-free and path-independent solution without displacement DOFs inside the patch, Comput. Methods Appl. Mech. Engrg. 373 (2021) 113437, http://dx.doi.org/10.1016/J.CMA.2020.113437.
[17] R. Pfefferkorn, S. Bieber, B. Oesterle, M. Bischoff, P. Betsch, Improving efficiency and robustness of enhanced assumed strain elements for nonlinear problems, Internat. J. Numer. Methods Engrg. 122 (8) (2021) 1911–1939, http://dx.doi.org/10.1002/nme.6605, URL https://onlinelibrary.wiley.com/doi/abs/10.1002/nme.6605.
[18] D. Magisano, L. Leonetti, G. Garcea, Advantages of the mixed format in geometrically nonlinear analysis of beams and shells using solid finite elements, Internat. J. Numer. Methods Engrg. 109 (9) (2017) 1237–1262, http://dx.doi.org/10.1002/nme.5322.
[19] L. Leonetti, G. Garcea, D. Magisano, F. Liguori, G. Formica, W. Lacarbonara, Optimal design of CNT-nanocomposite nonlinear shells, Nanomaterials 10 (12) (2020) 2484, http://dx.doi.org/10.3390/nano10122484, URL http://dx.doi.org/10.3390/nano10122484.
[20] D. Magisano, A. Corrado, New robust and efficient global iterations for large deformation finite element analysis of beams and shells with material nonlinearity, Comput. Methods Appl. Mech. Engrg. 406 (2023) 115900, http://dx.doi.org/10.1016/j.cma.2023.115900, URL https://www.sciencedirect.com/science/article/pii/S0045782523000233.
[21] F.S. Liguori, G. Zucco, A. Madeo, D. Magisano, L. Leonetti, G. Garcea, P.M. Weaver, Postbuckling optimisation of a variable angle tow composite wingbox using a multi-modal Koiter approach, Thin-Walled Struct. 138 (2019) 183–198, http://dx.doi.org/10.1016/j.tws.2019.01.035.
[22] F.S. Liguori, A. Madeo, D. Magisano, L. Leonetti, G. Garcea, Post-buckling optimisation strategy of imperfection sensitive composite shells using koiter method and Monte Carlo simulation, Compos. Struct. 192 (2018) 654–670, http://dx.doi.org/10.1016/j.compstruct.2018.03.023, URL http://www.sciencedirect.com/science/article/pii/S0263822317339776.
[23] F.S. Liguori, G. Zucco, A. Madeo, G. Garcea, L. Leonetti, P.M. Weaver, An isogeometric framework for the optimal design of variable stiffness shells undergoing large deformations, Int. J. Solids Struct. 210–211 (2021) 18–34, http://dx.doi.org/10.1016/j.ijsolstr.2020.11.003, URL https://www.sciencedirect.com/science/article/pii/S0020768320304261.
[24] F.S. Liguori, D. Magisano, A. Madeo, L. Leonetti, G. Garcea, A koiter reduction technique for the nonlinear thermoelastic analysis of shell structures prone to buckling, Internat. J. Numer. Methods Engrg. 123 (2) (2022) 547–576, http://dx.doi.org/10.1002/nme.6868, URL https://onlinelibrary.wiley.com/doi/abs/10.1002/nme.6868.
[25] J. Kiendl, M.-C. Hsu, M. Wu, A. Reali, Isogeometric Kirchhoff–Love shell formulations for general hyperelastic materials, Comput. Methods Appl. Mech. Engrg. 291 (2015) 280–303.

[26] L. Vu-Quoc, X.G. Tan, Optimal solid shells for non-linear analyses of multilayer composites. I Statics, Comput. Methods Appl. Mech. Engrg. 192 (9–10) (2003) 975–1016, http://dx.doi.org/10.1016/S0045-7825(02)00435-8.
[27] L. Vu-Quoc, X. Tan, Efficient Hybrid-EAS solid element for accurate stress prediction in thick laminated beams, plates, and shells, Comput. Methods Appl. Mech. Engrg. 253 (2013) 337–355, http://dx.doi.org/10.1016/j.cma.2012.07.025, URL http://dx.doi.org/10.1016/j.cma.2012.07.025.
[28] M. Schwarze, S. Reese, A reduced integration solid-shell finite element based on the EAS and the ANS concept—Geometrically linear problems, Comput. Methods Appl. Mech. Engrg. (80) (2009) 1322–1355, http://dx.doi.org/10.1002/nme.
[29] M. Schwarze, S. Reese, A reduced integration solid-shell finite element based on EAS and the ANS concept: Large deformation problems, Internat. J. Numer. Methods Engrg. (85) (2011) 289–329, http://dx.doi.org/10.1002/nme.
[30] L. Leonetti, D. Magisano, A. Madeo, G. Garcea, J. Kiendl, A. Reali, A simplified Kirchhoff–Love large deformation model for elastic shells and its effective isogeometric formulation, Comput. Methods Appl. Mech. Engrg. 354 (2019) 369–396, http://dx.doi.org/10.1016/j.cma.2019.05.025, URL http://www.sciencedirect.com/science/article/pii/S0045782519302956.
[31] D. Magisano, L. Leonetti, G. Garcea, Unconditional stability in large deformation dynamic analysis of elastic structures with arbitrary nonlinear strain measure and multi-body coupling, Comput. Methods Appl. Mech. Engrg. 393 (2022) 114776, http://dx.doi.org/10.1016/j.cma.2022.114776, URL https://www.sciencedirect.com/science/article/pii/S0045782522001190.
[32] T.J.R. Hughes, T.K. Caughey, W.K. Liu, Finite-element methods for nonlinear elastodynamics which conserve energy, J. Appl. Mech. 45 (2) (1978) 366–370, http://dx.doi.org/10.1115/1.3424303.
[33] J. Simo, N. Tarnow, K. Wong, Exact energy-momentum conserving algorithms and symplectic schemes for nonlinear dynamics, Comput. Methods Appl. Mech. Engrg. 100 (1) (1992) 63–116, http://dx.doi.org/10.1016/0045-7825(92)90115-Z.
[34] J. Simo, N. Tarnow, The discrete energy-momentum method. Conserving algorithms for nonlinear elastodynamics, Z. Angew. Math. Phys. ZAMP 43 (1) (1992) 757–792, http://dx.doi.org/10.1007/BF00913408.
[35] N. Tarnow, J. Simo, How to render second order accurate time-stepping algorithms fourth order accurate while retaining the stability and conservation properties, Comput. Methods Appl. Mech. Engrg. 115 (3) (1994) 233–252, http://dx.doi.org/10.1016/0045-7825(94)90061-2, URL https://www.sciencedirect.com/science/article/pii/0045782594900612.
[36] J.C. Simo, N. Tarnow, A new energy and momentum conserving algorithm for the non-linear dynamics of shells, Internat. J. Numer. Methods Engrg. 37 (15) (1994) 2527–2549, http://dx.doi.org/10.1002/nme.1620371503, URL https://onlinelibrary.wiley.com/doi/abs/10.1002/nme.1620371503.
[37] Error bounds for finite element method, Numer. Math. 16 (1971) 322–333.
[38] On the existence, uniqueness and approximation of saddle-point problems arising from Lagrange multipliers, RAIRO Anal. Numer. 8 (1974) 129–151.
[39] P.J. Flory, Thermodynamic relations for high elastic materials, Trans. Faraday Soc. (1961) http://dx.doi.org/10.1039/TF9615700829.
[40] P. Wriggers, Nonlinear Finite Element Methods, 2008, http://dx.doi.org/10.1007/978-3-540-71001-1, arXiv:1011.1669v3.
[41] A.G. Holzapfel, Nonlinear Solid Mechanics, John Wiley Sons, New-York, 2000.
[42] N. Büchter, E. Ramm, D. Roehl, Three-dimensional extension of non-linear shell formulation based on the enhanced assumed strain concept, Internat. J. Numer. Methods Engrg. 37 (15) (1994) 2551–2568, http://dx.doi.org/10.1002/nme.1620371504, URL https://onlinelibrary.wiley.com/doi/abs/10.1002/nme.1620371504.
[43] N.M. Newmark, A method of computation for structural dynamics, J. Eng. Mech. Div. 85 (3) (1959) 67–94, http://dx.doi.org/10.1061/JMCEA3.0000098, arXiv:https://ascelibrary.org/doi/pdf/10.1061/JMCEA3.0000098, URL https://ascelibrary.org/doi/abs/10.1061/JMCEA3.0000098.
[44] J. Kiendl, K.-U. Bletzinger, J. Linhard, R. W., Isogeometric shell analysis with Kirchhoff–Love elements, Comput. Methods Appl. Mech. Engrg. 198 (49) (2009) 3902–3914, http://dx.doi.org/10.1016/j.cma.2009.08.013, URL http://www.sciencedirect.com/science/article/pii/S0045782509002680.